Spectroscopic Definition of the Cu_Z^o Intermediate in Turnover of Nitrous Oxide Reductase and Molecular Insight into the Catalytic Mechanism

Esther M. Johnston,[#,†] Cíntia Carreira,[%] Simone Dell'Acqua,[%,‡] Somdatta Ghosh Dey,[#,&] Sofia R. Pauleta,[%] Isabel Moura,[%] and Edward I. Solomon[#,*]

[#]Department of Chemistry, Stanford University, Stanford, CA. [%]UCIBIO, REQUIMTE, Departamento de Química, Faculdade de Ciências e Tecnologia, Universidade Nova de Lisboa, Campus da Caparica, 2829-516 Caparica, Portugal.

Keywords: *Nitrous oxide reductase; active form; catalytic cycle; Cu_Z center; Copper enzyme; Intermediate species*

ABSTRACT: Spectroscopic methods and density functional theory (DFT) calculations are used to determine the geometric and electronic structure of Cu_Z^o, an intermediate form of the Cu_4S active site of nitrous oxide reductase (N_2OR) that is observed in single turnover of fully reduced N_2OR with N_2O. Electron paramagnetic resonance (EPR), absorption, and magnetic circular dichroism (MCD) spectroscopies show that Cu_Z^o is a 1-hole (i.e. $3Cu^ICu^{II}$) state with spin density delocalized evenly over Cu_I and Cu_{IV}. Resonance Raman spectroscopy shows two Cu-S vibrations at 425 and 413 cm^{-1}, the latter with a -3 cm^{-1} O^{18} solvent isotope shift. DFT calculations correlated to these spectral features show that Cu_Z^o has a terminal hydroxide ligand coordinated to Cu_{IV}, stabilized by a hydrogen bond to a nearby lysine residue. Cu_Z^o can be reduced via electron transfer from Cu_A using a physiologically relevant reductant. We obtain a lower limit on the rate of this intramolecular electron transfer (IET) that is $>10^4$ faster than the unobserved IET in the resting state, showing that Cu_Z^o is the catalytically relevant oxidized form of N_2OR. Terminal hydroxide coordination to Cu_{IV} in the Cu_Z^o intermediate yields insight into the nature of N_2O binding and reduction, specifying a molecular mechanism in which N_2O coordinates in a μ-1,3 fashion to the fully reduced state, with hydrogen bonding from Lys397, and two electrons are transferred from the fully reduced μ_4S^{2-} bridged tetranuclear copper cluster to N_2O via a single Cu atom to accomplish N-O bond cleavage.

1. Introduction.

The mitigation of man-made pollution of the global atmosphere is one of the most important scientific challenges of the 21st century. Nitrous oxide (N_2O) emissions from anthropogenic sources are important contributors to global warming, as N_2O has 300 times the global warming potential of CO_2,[1] and also contributes to the depletion of the ozone layer.[2] Two-thirds of anthropogenic N_2O emissions arise from agricultural soils,[3,4] where N_2O is formed as part of the bacterial denitrification pathway, in which soil and marine bacteria use oxidized nitrogen compounds as terminal electron acceptors for anaerobic respiration.[5] Many bacterial denitrifiers contain the enzyme nitrous oxide reductase (N_2OR), which catalyzes the two electron and two proton reduction of N_2O to N_2 and H_2O, as the terminal step of denitrification, thus preventing the environmental release of N_2O.[6,7] This reaction is exergonic by 81 kcal/mol but kinetically hindered by a high barrier for N-O bond cleavage (+59 kcal/mol in the gas phase), thus requiring enzymatic catalysis.[8] Understanding the molecular mechanism by which N_2OR catalyzes this reaction *in vivo* could contribute to efforts to mitigate the environmental release of N_2O.[3]

N_2OR is a homodimeric metalloenzyme that contains two copper sites: a binuclear copper site known as Cu_A, which receives an electron from cytochrome *c* or cupredoxin and transfers it to a unique tetranuclear copper monosulfide

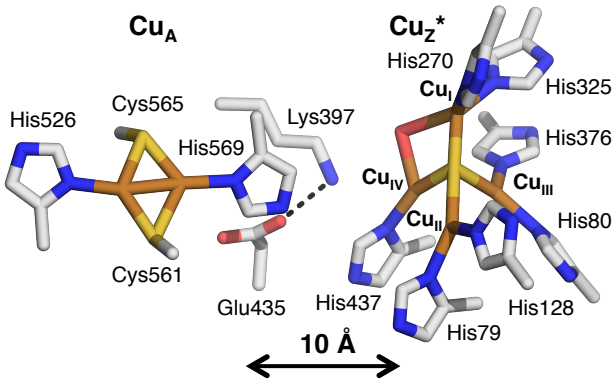

Figure 1: A) X-ray crystallographic structure of the copper sites of nitrous oxide reductase from *Paracoccus denitrificans* (1FWX, resolution 1.7 Å),[9] identifying important ligating and second sphere residues.

(Cu_4S) active site, where N_2O binds and is reduced (Figure 1).[9-13] The two copper sites are separated by a distance of 10 Å across the dimer interface and a solvent-filled cavity lies between them. Cu_A is ligated equatorially by two bridging Cys and two His residues and is structurally and electronically similar to an equivalent electron transfer site in the enzyme cytochrome *c* oxidase.[14,15] The Cu_4S active site is ligated by 7 His residues and contains three copper atoms (designated Cu_I, Cu_{II}, and Cu_{IV}) that share a plane with the μ_4

sulfide ligand and with a solvent-derived ligand that bridges the Cu_I-Cu_{IV} edge, while the fourth copper (Cu_{III}) bound to the μ_4S^{2-} is oriented out of this plane. The resting state of the Cu_4S cluster, known as Cu_Z*, has been extensively characterized by spectroscopic methods and has a mixed valent $3Cu^{I}$-Cu^{II} (1- hole) electronic structure, where the hole is delocalized in a ~5:2 ratio over two coppers in the cluster, Cu_I and Cu_{IV}, respectively.[16-19] Studies of the pH dependence of the resting 1-hole Cu_Z* state show that in this state the solvent-exchangeable Cu_I-Cu_{IV} edge ligand is a hydroxide, which changes position depending on the protonation state of the second sphere residue Lys397 (Figure 1).[20] An alternative two sulfur (Cu_4S_2) form of the N_2OR active site has been observed when N_2ORs from *Pseudomonas stutzeri* and *Marinobacter hydrocarbonoclasticus* (*Mh*N_2OR, used in this study) are isolated under low dioxygen conditions.[21,22] However, single turnover studies have shown that none of the accessible redox states of the Cu_4S_2 cluster react rapidly with N_2O,[23] while the fully reduced ($4Cu^{I}$) state of the Cu_4S cluster does react with N_2O at a sufficiently rapid rate to be catalytically relevant.[24] The $4Cu^{I}$ state of the Cu_4S cluster is also responsible for turnover in the standard steady-state assay for N_2OR activity, which uses the electron donor methyl viologen.[23,25]

Despite the evidence that the $4Cu^{I}$ state of the Cu_4S cluster is the only form of the N_2OR active site that can reduce N_2O at a rate that is catalytically competent for turnover,[23] important questions remain. Specifically, the putative reactive $4Cu^{I}$ state can only be accessed *in vitro* from the resting 1-hole Cu_Z* state via a slow reductive activation using dithionite-reduced viologen reductants (methyl or benzyl viologen), and not with physiologically relevant reductants, such as cytochrome c_{552}, the physiological electron donor of *Mh*N_2OR, or sodium ascorbate.[25,26] This calls into question whether the reactive $4Cu^{I}$ state of the Cu_4S cluster can be accessed *in vivo*; indeed, the reduction of resting 1-hole Cu_Z* to the $4Cu^{I}$ state is too slow to be part of the catalytic cycle. However, an alternative oxidized state of the Cu_4S cluster, known as Cu_Z^o, has been observed as a transient intermediate in the single turnover reaction of fully reduced N_2OR with N_2O.[27] In contrast to resting 1-hole Cu_Z*, Cu_Z^o is reduced rapidly in steady-state experiments with methyl viologen. The Cu_Z^o intermediate shows an S=½ EPR signal, indicating that it is a 1-hole state of the Cu_4S cluster, and an absorption maximum at 680 nm, red-shifted from the absorption maximum of resting 1-hole Cu_Z*, which is at 640 nm.[27] Characterization of the Cu_Z^o intermediate to determine its geometric and electronic structure and reactivity with physiologically relevant reductants is essential to elucidate how it differs from the resting 1-hole form of Cu_Z* and understand its role in the mechanism of N_2O reduction.

In this study, EPR, absorption, MCD, and resonance Raman spectroscopies are performed on freeze-trapped samples of the Cu_Z^o intermediate to characterize its electronic structure. We then use DFT calculations to develop a structural model for this intermediate that is consistent with this electronic structure and with the differences in spectral features of Cu_Z^o relative to resting 1-hole Cu_Z*. We further determine that the Cu_Z^o intermediate can be rapidly reduced to the reactive $4Cu^{I}$ state via electron transfer from Cu_A using a physiologically relevant reductant, sodium ascorbate, and use our computational model to elucidate the structural and energetic basis for the rapid reduction of Cu_Z^o but not of the resting 1-hole Cu_Z* by Cu_A in turnover. This establishes that the Cu_Z^o intermediate is the relevant 1-hole oxidized form of the Cu_4S cluster in the turnover and reduction of N_2O, bypassing the inactive resting 1-hole Cu_Z* state. We further extend the structural insight gained from the Cu_Z^o intermediate to examine the nature of the two electron reduction of N_2O performed by the Cu_4S cluster, the key catalytic role of the N_2OR active site.

2. Methodology.

2.1 Materials: All reagents were of the highest grade commercially available and used without further purification. Buffers and reductants were purchased from Sigma-Aldrich. 10% N_2O in argon was obtained from Praxair. D_2O (99.9% D), deuterated glycerol (98% D), and H_2O^{18} (97% O^{18}) were purchased from Cambridge Isotopes.

2.2 Isolation of nitrous oxide reductase: Nitrous oxide reductase was purified from *Marinobacter hydrocarbonoclasticus* 617 (previously named *Pseudomonas nautica*) according to previously published procedures.[22] The cells were grown anaerobically in the presence of nitrate, and *Mh*N_2OR was purified under aerobic conditions without added reductant, using a three step column procedure that has been shown to result in *Mh*N_2OR that contains dominantly the monosulfide Cu_4S, resting 1-hole Cu_Z*, cluster, with the presence of a minimal amount of the disulfide Cu_4S_2 form.[22,23] The amount of the Cu_4S cluster present in the purified *Mh*N_2OR used for this study was determined by EPR spin quantitation before and after methyl viologen reduction (which results in reduction of all copper sites except the 1-hole state of the Cu_4S_2 cluster). 90±10% or 80±10% of the total tetranuclear cluster concentration was determined to be the Cu_4S form and 10±10% or 20±10% was determined to be the Cu_4S_2 form of the cluster. The purified enzyme was stored in 100 mM Tris-HCl at a pH 7.6 in liquid nitrogen until further use. The two enzyme preparations used in this study have specific activities of 180 ± 17 and 190 ± 20 μmol $N2O\ min^{-1}\ mg^{-1}$ for the 80% and 90% Cu_4S *Mh*N_2OR, respectively, at pH 7.6.

2.3 Spectroscopic sample preparation and instrumentation: Fully reduced Cu_4S-containing *Mh*N_2OR samples were prepared in a glove box under N_2 atmosphere. *Mh*N_2OR in 100 mM pH 7.6 phosphate buffer was reduced by incubation with a 100-fold excess of sodium dithionite-reduced methyl viologen. After 1-2 hours of reduction, the excess reductant was removed by PD-10 Sephadex G-25 desalting column and the protein-containing fractions were concentrated by centrifugation. Fully reduced samples were transferred out of the glove box in tightly capped absorption cuvettes, conical vials, or EPR tubes and immediately used for spectroscopic sample preparation.

The reaction of fully reduced *Mh*N_2OR with N_2O was initiated by adding a stoichiometric amount of N_2O from a solution of 2.5 mM N_2O in 100 mM pH 7.6 phosphate buffer, obtained by saturation of the buffer with 10% N_2O in argon at room temperature. 10-15 μL of the 2.5 mM N_2O solution were typically added to ~250 μL of fully reduced *Mh*N_2OR for 0.10-0.30 mM concentrations of Cu_Z^o. Complete mixing was obtained by vigorously shaking or vortexing the

reaction mixture for 15-30 seconds. Absorption spectra of Cu_Z^o were obtained by performing the N_2O reaction in a quartz cuvette at room temperature. The reaction progress was monitored with an Agilent 8453 UV-vis spectrophotometer with deuterium and tungsten sources. The first absorption spectrum of Cu_Z^o was obtained at 30 seconds after the initial addition of N_2O.

Samples for electron paramagnetic resonance (EPR) and resonance Raman spectroscopy of Cu_Z^o were prepared by carrying out the N_2O reaction with 0.1-0.5 mM fully reduced N_2OR in a quartz EPR tube, which was vortexed for 15-30 seconds and immediately frozen in an acetone/dry ice bath. After freezing, samples were transferred to liquid nitrogen for storage and data collection. X band EPR spectra were collected using a Bruker EMX spectrometer with an ER 041 XG microwave bridge and an ER4102ST sample cavity. X-band samples were run at 77 K using a liquid nitrogen finger dewar. EPR spectra were baseline corrected using the WinEPR program (Bruker) and simulated using the XSophe program (Bruker). Resonance Raman spectra were collected using a series of lines from a Kr^+ ion laser (Coherent 190CK), a Ti-sapphire laser (M-squared SolsTice, pumped by a 12 W Lighthouse Photonics Sprout diode pumped solid state laser), and a Dye laser (Rhodamine 6G, Coherent 699) with incident power of 20-30 mW arranged in a 130° backscattering configuration. The scattered light was dispersed through a triple monochromator (Spex 1877 CP, with 1200, 1800, and 2400 grooves mm^{-1} gratings) and detected with a back-illuminated CCD camera (Andor iDus model). Samples prepared in EPR tubes were immersed in a liquid nitrogen finger dewar at 77 K for resonance Raman experiments. The intensity of the ice peak at ~229 cm^{-1} was used to normalize the intensities of vibrations to obtain resonance Raman excitation profiles. The spectrum of carbon black in an identical quartz EPR tube was subtracted to remove the spectral contribution from quartz scattering.

Samples for magnetic circular dichroism (MCD) spectroscopy were prepared by premixing 0.1-0.3 mM fully reduced *Mh*N_2OR with 50% deuterated glycerol and preparing a 2.5 mM N_2O solution in 1:1 deuterated glycerol to 100 mM phosphate buffer at pD 7.6. Upon addition of a stoichiometric amount of the N_2O solution to fully reduced *Mh*N_2OR in 50% glycerol, the reaction was mixed with a syringe for ~30 s, then transferred to an MCD cell and frozen in an acetone/dry ice bath at -80°C. Parallel MCD samples of fully reduced *Mh*N_2OR were prepared by adding glycerol-buffer solutions that did not contain N_2O. These were used to determine the spectral contribution of the residual unreduced 1-hole Cu_4S_2 cluster. MCD spectra were collected on CD spectro-polarimeters (Jasco J810 with an S20 PMT detector for the 300-900 nm region and a Jasco J730 with an InSb detector for the 600-2000 nm region) with sample compartments modified to insert a magnetocryostat (Oxford Instruments SM4-7T).

2.4 Reactivity and steady-state kinetics: Fully reduced N_2OR was prepared by incubation with 100 equivalents of reduced methyl viologen in 100 mM Tris-HCl pH 7.6 for 3 hours. Reductants were removed in a NAP-5 column equilibrated with 100 mM pH 7.6 phosphate buffer and the protein concentration was determined by the Pierce Method. To study the reduction of Cu_Z^o by sodium ascorbate, typically 20 μM fully reduced N_2OR was reacted with 36 μM N_2O to form Cu_Z^o in a stirred absorption cell. After 37 seconds of reaction with N_2O, a solution containing sodium ascorbate was added (final concentration of 7.29 mM, 366-fold molar excess) to the cuvette under agitation. The reduction was followed by absorption spectroscopy, using a TIDAS diode-array spectrophotometer and spectra were collected for at least 1 hour inside a Mbraun anaerobic box. A parallel experiment using sodium ascorbate to reduce *Mh*N_2OR containing resting 1-hole Cu_Z* and oxidized Cu_A was performed as above with 16.5 μM N_2OR and 7.5 mM sodium ascorbate. An additional experiment was performed in which fully reduced N_2OR was added to a stirred cell containing sodium ascorbate and N_2O (final concentrations: 20 μM N_2OR, 10 mM ascorbate, and 0.2 mM N_2O). Control experiments to monitor changes in fully reduced N_2OR in the absence and presence of sodium ascorbate were also performed (no absorbance changes was observed over time, data not shown). All these experiments were performed with a sample of *Mh*N_2OR containing 80% of the Cu_4S and 20% of the Cu_4S_2 cluster.

The dependence of the steady-state activity of *Mh*N_2OR on pH, pD, and temperature was determined. Steady-state activity measurements were performed by monitoring the oxidation of reduced methyl viologen, following published procedures.[10] *Mh*N_2OR (~0.2 mM) was activated in a glove box under nitrogen atmosphere by incubation for 1.5 hours with 500 equivalents of dithionite-reduced methyl viologen at pH 8.0. A solution of 1 mL dithionite-reduced methyl viologen (2.8 mM) was prepared in an anaerobic cuvette at the appropriate pH, pD, or temperature, and an aliquot of the reduced *Mh*N2OR solution was added to the cuvette under stirring. 20 μL of N_2O saturated water (25 mM) was immediately added to initiate the steady-state turnover reaction (final concentrations: [N_2OR] ~ 4 μM, [N_2O] ~ 500 μM, [MV] ~ 2.8 mM). There is a 10% error in activity measurements obtained by this method. The buffers used for the pH/pD profile were MES (pH 5.5-6.5), phosphate (pH 7-8), CHES (pH 8.5-9.5) and CAPS (pH 10-10.5). Typically 3 replicates were performed at each pH and pD, while six replicates were performed at each temperature. pH and pD activity values reported are the average of multiple replicates with the appropriate propagation of errors. The log of the initial rate of oxidation of reduced methyl viologen (k or k/T) was plotted relative to 1/T to obtain thermodynamic parameters for the rate determining step of steady-state turnover in *Mh*N_2OR.

2.5 Computational Methods: A computational model of the Cu_4S active site was built from the atomic coordinates of the crystal structure of *Pd*N_2OR (PDB ID 1FWX, residue numbers from *Mh*N_2OR), as it is the highest resolution structure available of N_2OR (resolution 1.6 Å). The model included the active site core (Cu_4S), the edge hydroxide, 7 ligating histidines, and the second sphere residues Lys397 and Glu435 (Figure 1). All protein residues were included up to the α carbons, which were constrained at their crystallographic positions. The distal nitrogen of each His ligand, which is typically involved in a hydrogen bond to a second sphere residue or the protein backbone, was also fixed in place. Additionally, the distant oxygen of Glu435 was constrained in its crystallographic position. (In optimizations

including an unconstrained Glu435, this residue moves significantly from its crystallographic position to form a hydrogen bond to His437, a Cu_{IV} ligand.) Calculations were performed using Gaussian 09 (version d01).[28] Molecular structures and frequencies were visualized using Avogadro, an open source molecular builder and visualization tool (Version 1.1.1).[29] LUMO version 1.0.3[30] and VMD 1.9.1[31] were used to visualize molecular orbitals and QMForge was used to obtain Mulliken spin populations of different orbitals.[32] Geometry optimizations were performed using B3LYP and BP86 with 10% Hartree-Fock exchange, the TZVP basis set on all core atoms (Cu_4S), the ligating His nitrogens, the edge ligand and atoms involved in the Lys397-Glu435 hydrogen bonding network (NH_3^+ or NH_2 of Lys397 and CO_2 of Glu435), and the SV basis set on all remaining atoms. Optimizations were performed in a PCM of 10 to ensure that the proton involved in the Lys397-Glu435 hydrogen bond remains on Lys397 (PCM values less than 8 yield a neutral Lys397 Glu435-H as the lowest energy structure). Optimized structures were then used for frequency calculations. In the analysis of vibrational frequencies of the Cu_I-OH_2-Cu_{IV} and Cu_{IV}-OH models of Cu_Z^o, significant mixing was observed between high energy Cu-S stretching modes and His methylene bending modes. To remove this computational artifact, the α carbons of His residues involved in this mixed were increased in mass until pure Cu-S vibrations were obtained.[33]

The decay process of the Cu_{IV}-OH model of Cu_Z^o to resting 1-hole Cu_Z*, with an OH bridged edge, was calculated by performing a 1D potential energy scan with a constrained Cu_I-OH and Cu_I-Cu_{IV} distance of 3.6 Å (to reflect the larger Cu_I-Cu_{IV} distance observed crystallographically for resting Cu_Z*) and a transition state was obtained for this process. The process is close to barrier-less when the Cu_I-Cu_{IV} distance is not constrained.

To obtain a starting structure for the N-O bond cleavage coordinate, N_2O was positioned near an optimized fully reduced model of the cluster.[8,34] Initial geometries investigated included μ-1,3 coordination of N_2O (with the O on both Cu_I and Cu_{IV}), μ-1,1-O coordination, and terminal coordination of a linear N_2O molecule to Cu_I or Cu_{IV} through either the N or O. Stationary points were only found for end-on N coordination to Cu_I and for μ-1,3 bent coordination with the O coordinated to Cu_{IV} (using BP86 with 10% Hartree-Fock; B3LYP has no stationary point for this structure). In the N-O bond elongation coordinate for the terminal Cu_I-N_2O structure, the N_2O molecule undergoes an early rearrangement with no barrier to form a μ-1,3 coordinated bent N_2O that proceeds in N-O bond cleavage as found for the μ-1,3 structure obtained with BP86 and 10% Hartree-Fock. The μ-1,3 bound N_2O structure obtained with BP86 and 10% Hartree-Fock exchange was used as the starting point for a 1D potential energy scan of N-O bond elongation, leading to a transition state for this process. The μ-1,3 N_2O structure was also used to generate 2D and 3D potential energy surfaces for N-O bond cleavage, proton transfer from Lys397 to O, and Cu_I-N bond cleavage.

3. Results and Analysis.

3.1 Spectroscopy of Cu_Z^o: The reaction of fully reduced *Mh*N_2OR with stoichiometric N_2O (in the absence of additional reductant) results in the rapid formation of the intermediate Cu_Z^o, concomitant with oxidation of Cu_A.[27] The kinetics of formation (k_f = 200 s^{-1})[23] and decay (k_{decay} = 0.005 s^{-1})[27], previously reported for the Cu_Z^o intermediate, indicate that samples trapped in less than two minutes will contain mainly Cu_Z^o (Figure S1). Accounting for all the species in the reaction mixture, spectra of samples trapped in 50-60 s (Figure S2, black) contain contributions from three species: the Cu_Z^o intermediate (68%), oxidized Cu_A (68%), and residual 1-hole Cu_4S_2 Cu_Z (~10% present for the N_2OR preparation used here). The spectral features of Cu_Z^o were cleanly distinguished from the mixtures by removing the spectral contributions of 1-hole Cu_Z and oxidized Cu_A. The spectral contribution of residual 1-hole Cu_4S_2 Cu_Z was determined from samples of the methyl viologen reduced protein (shown in Ref. [23] to reduce all copper sites except the 1-hole Cu_4S_2 Cu_Z cluster) that were prepared in parallel with the intermediate samples (Figure S2, blue). The spectral contribution of oxidized Cu_A was determined by subtracting the spectrum of oxidized resting *Mh*N_2OR from that of ascorbate-reduced *Mh*N_2OR (which from Ref. [23] reduces only Cu_A) and scaling the resulting Cu_A spectrum to the appropriate concentration (Figure S2, red). For the EPR and MCD spectra, fit versions of the Cu_A spectra were used for these subtractions.

3.1.1 EPR: The X band EPR spectrum of Cu_Z^o obtained using this approach is axial with $g_{||} > g_\perp > 2.0023$, indicating a $d_{x^2-y^2}$ ground state. Six hyperfine features can be discerned, showing that the unpaired spin is delocalized over more than one Cu (Figure 2, black, with simulation shown in red).

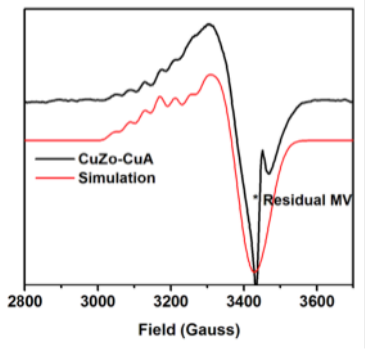

Figure 2: EPR spectrum of Cu_Z^o at 77 K (black) after subtraction of 1-hole Cu_Z and an equal spin integration of oxidized Cu_A, with fit (red). MV, reduced methyl viologen.

The EPR spectrum of Cu_Z^o was fit with similar g values to those previously obtained for resting 1-hole Cu_Z* (Table 1), consistent with the results obtained by Dell'Acqua et. al.[27] However, we are additionally able to resolve the $A_{||}$ hyperfine features of Cu_Z^o. Two equal $A_{||}$ values are required to fit the hyperfine pattern, reflecting an equal distribution of spin over two coppers, while in resting Cu_Z* two unequal $A_{||}$ values are required, reflecting a spin distribution over two coppers of ~5:2 in the resting state.[35] This indicates that the unpaired.

Table 1: g and A values obtained from fitting the X band EPR spectra of Cu_Z^o and resting 1-hole Cu_Z* values from Ref. [35], with $g_\perp$ estimated from the crossover point.

	Cu_Z^o	Cu_Z*
$g_{\|\|}$	2.177	2.160
$A_{\|\|}$	42×10^{-4} cm^{-1} 42×10^{-4} cm^{-1}	61×10^{-4} cm^{-1} 23×10^{-4} cm^{-1}
$g_\perp$	~2.05	2.042

spin in the Cu_Z^o intermediate has shifted from being mostly localized on Cu_I, as in resting 1-hole Cu_Z*, to being more equally delocalized over two different coppers.

3.1.2 Absorption and MCD: The absorption spectrum of Cu_Z^o, obtained after the subtraction of the contributions of oxidized Cu_A and 1-hole Cu_Z, shows an asymmetrically shaped intense peak maximum at ~14,900 cm^{-1} ($\varepsilon \approx 2000$ M^{-1} cm^{-1}, Figure 3A) with a shoulder to higher energy. This absorption maximum is lower in energy by ~700 cm^{-1} than that of resting 1-hole Cu_Z* (shown for comparison in Figure 3B). The absorption maximum correlates to a derivative shaped pseudo-A feature in the MCD spectrum of Cu_Z^o comprised of a negative band at 14,200 cm^{-1} and a positive band at 15,900 cm^{-1} (Figure 3A, bands 5 and 6 respectively, band numbers taken from the fit of resting 1-hole Cu_Z* in Ref. [20]). Simultaneous fitting of the absorption and MCD spectra of Cu_Z^o yields 6 transitions that can be clearly identified, which are assigned as d-d (band 3), μ_4S^{2-} to Cu charge transfer (CT, bands 5, 6 and 7), and His to Cu CT transitions (bands 9-10) based on their energies and C_0/D_0 ratios following Ref. [20] (Table S1). The transitions that contribute to the absorption maximum and pseudo-A feature are μ_4S^{2-} to Cu CT transitions that occur at very similar energies to the equivalent transitions (5 and 6) in resting 1-hole Cu_Z* (Table S1). Thus, while the absorption maximum of Cu_Z^o appears to be at lower energy than in resting 1-hole Cu_Z*, this is due to a change in the *relative intensities* of the μ_4S^{2-} to Cu CT transitions, not a shift in their energies. A recent study of the intensities of the μ_4S^{2-} to Cu CT transitions in resting 1-hole Cu_Z* and 1-hole Cu_4S_2 Cu_Z has shown that these intensities reflect the overlap of the three perpendicular S p orbitals with the β LUMO of the cluster (Figure S3), such that a higher intensity for band 5 reflects more spin delocalization onto Cu_{IV} in the β LUMO while band 6 reflects the spin on Cu_I.[36] Thus, the change in relative intensities of the μ_4S^{2-} to Cu CT transitions in Cu_Z^o relative to resting 1-hole Cu_Z*, where band 6 decreases in intensity while band 5 increases, indicates that there is less spin on Cu_I and more spin on Cu_{IV} in the Cu_Z^o intermediate. This confirms and provides insight into the observation from the EPR $A_{\|\|}$ values that the spin density of the Cu_Z^o intermediate cluster has shifted from being distributed ~5:2 on Cu_I and Cu_{IV} in resting 1-hole Cu_Z* to being more delocalized to a second Cu (from MCD, Cu_{IV}) in Cu_Z^o. A direct way to accomplish this shift in spin density is to change the nature or position of the Cu_I-Cu_{IV} edge ligand in the Cu_Z^o relative to the μOH ligand in resting 1-hole Cu_Z*, such that the ligand field on Cu_I is decreased and the ligand field on Cu_{IV} is increased, leading to a shift of some of the spin density from Cu_I onto Cu_{IV}.

3.1.3 Resonance Raman: Upon laser excitation into the absorption maximum of Cu_Z^o, two features are resonance enhanced in the Raman spectrum, an intense vibration at 426

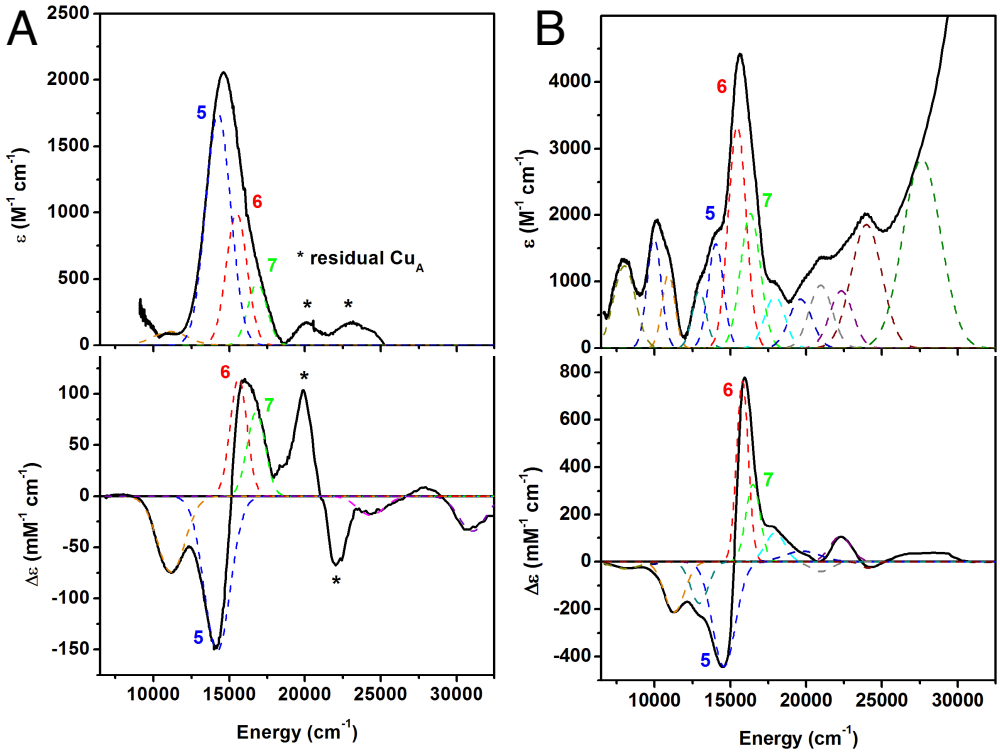

Figure 3: Absorption and MCD spectra of A) Cu_Z^o, absorption at 273 K and MCD at 5 K and 7 T, and B) resting Cu_Z*, absorption at 5 K and MCD at 5 K, 7 T, showing the Gaussian bands obtained from a simultaneous fit, following the fit for Cu_Z* from Ref. [17].

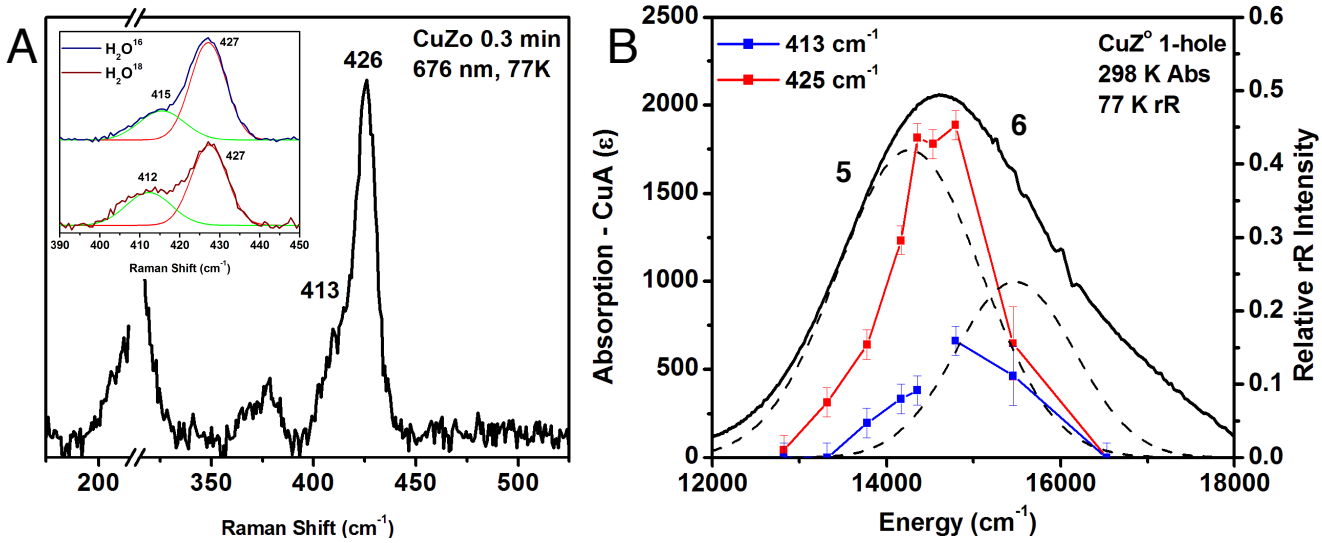

Figure 4: Resonance Raman spectrum and profile of Cu_Z^o, obtained after 15 s of reaction with N_2O. A) Spectrum at 77 K, excitation energy 676 nm. Inset: O^{16}/O^{18} isotope perturbation observed after formation of Cu_Z^o in H_2O^{16} or H_2O^{18} 100 mM phosphate at pH 7.6. The O^{16}/O^{18} isotope data were fit with two bands of identical width, where in the O^{18} spectrum green band decreases in energy by 3 cm^{-1} and has 36% more intensity. B) Left scale: Room temperature absorption of Cu_Z^o at 30 s (after subtraction of oxidized Cu_A and 1-hole Cu_Z contributions). Right scale: Dependence of the normalized intensity of the vibrations of Cu_Z^o on excitation energy.

cm^{-1} and a weaker shoulder at 413 cm^{-1} (Figure 4A). These vibrations profile in the most intense μ_4S^{2-} to Cu CT transition (band 5), indicating that they are Cu-S stretching vibrations (Figure 4B). These Cu-S stretching vibrations occur at higher energy than those observed for resting 1-hole Cu_Z*, which has an intense Cu-S stretch at 378 cm^{-1} and a weaker Cu-S stretch at 362 cm^{-1} that profile similarly to the vibrations of Cu_Z^o (in band 6, the most intense S to Cu CT transition in Cu_Z*, Figure S4). This indicates that some of the Cu-S bonds are stronger in the Cu_Z^o intermediate relative to resting 1-hole Cu_Z*. Resting 1-hole Cu_Z* shows an additional Cu-S stretch at 412 cm^{-1} that profiles differently (in the third sulfide to Cu CT transition, band 7), which is not observed in Cu_Z^o due to the low intensity of band 7 in Cu_Z^o. When the Cu_Z^o intermediate is formed in H_2O^{18} buffer, the 413 cm^{-1} vibration shifts down in energy by 3 cm^{-1} and increases in intensity by ~36%, while the 426 cm^{-1} vibration remains unperturbed (Figure 4A, inset). Resting 1-hole Cu_Z* also shows some H_2O^{18} isotope sensitivity in the Cu-S stretch at 412 cm^{-1} (-9 cm^{-1}) but only at high pH. This H_2O^{18} sensitivity in resting 1-hole Cu_Z* has been previously assigned as coupling between a Cu-S core stretch and the Cu-O stretch of a hydroxide ligand that bridges the Cu_I-Cu_{IV} edge.[20] The position of the edge hydroxide ligand is perturbed by the protonation state of Lys397, such that the edge ligand stretch only shows kinematic coupling to the core stretch at high pH (the hydroxide ligand is present in resting 1-hole Cu_Z* at both high and low pH).[20] The presence of a similar H_2O^{18} isotope shift in the 413 cm^{-1} Cu-S stretch of the Cu_Z^o intermediate at neutral pH indicates that a solvent-exchangeable hydroxide edge ligand is also present in Cu_Z^o, since only the Cu-O stretches of a hydroxide will be high enough in energy to mix with the core Cu-S stretches of the cluster. The possibility of either a water or a hydroxide solvent-derived edge ligand is computationally evaluated below, and only a hydroxide ligand predicts H_2O^{18} isotope sensitivity in a high energy Cu-S vibration. Thus, the presence of H_2O^{18} sensitivity in the 413 cm^{-1} Cu-S core vibration indicates that the Cu_Z^o intermediate has a hydroxide ligand on the Cu_I-Cu_{IV} edge, similar to resting 1-hole Cu_Z* but differing in the position of the edge ligand (from the change in spin density by EPR and MCD).

3.2 Kinetics.

3.2.1 Reduction of Cu_Z^o versus 1-hole Cu_Z*: It has been reported previously that Cu_Z^o is competent to be involved in rapid turnover, since the steady-state activity of *Mh*N_2OR decays at the same rate as the decay of the Cu_Z^o intermediate to resting 1-hole Cu_Z*.[27] This suggests that the reduction of Cu_Z^o under steady-state turnover conditions occurs with a rate equal to or faster than k_{cat} (320±20 s^{-1} for *Mh*N_2OR, used in this study).[26] However, the reductant used in these assays, dithionite-reduced methyl viologen, is not physiologically relevant. To resolve this issue, we investigated whether Cu_Z^o can be reduced by the milder, physiologically relevant reductant sodium ascorbate. The reduction of Cu_Z^o upon addition of sodium ascorbate could be confirmed by resonance Raman spectroscopy, which shows that several minutes after addition of sodium ascorbate the vibrations at 426 and 413 cm^{-1} associated with Cu_Z^o disappear (Figure S5) indicating that, unlike resting 1-hole Cu_Z*, the Cu_Z^o intermediate can be reduced by sodium ascorbate.

For kinetic studies using absorption spectroscopy on a faster timescale, Cu_Z^o was formed *in situ* through the reaction of fully reduced N_2OR with close to stoichiometric N_2O, and a ~400-fold excess of sodium ascorbate was subsequently added (e.g., 7.3 mM sodium ascorbate, 20 μM *Mh*N_2OR). Addition of sodium ascorbate to Cu_Z^o leads to rapid decay of both the absorption maximum of Cu_Z^o at 14,900 cm^{-1} (Figure 5A and 5B, red) and the characteristic absorption features of oxidized Cu_A (20,800, 18,800, and 12,200 cm^{-1}, Figure 5A and 5B, blue) in the first 800 seconds, with slightly faster reduction of Cu_Z^o relative to Cu_A (Figure 5B). This behavior is

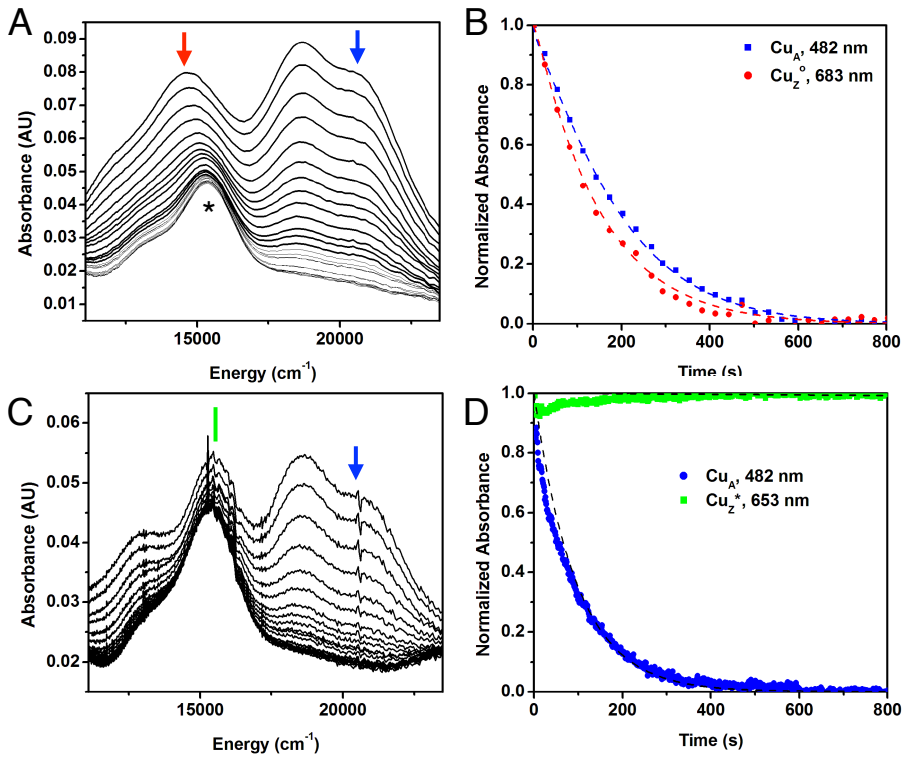

Figure 5: Sodium ascorbate reduction of Cu_Z^o and resting 1-hole Cu_Z*. A) Absorption spectra of the reduction of Cu_Z^o (red arrow) and oxidized Cu_A (blue arrow) by 7.3 mM (~400 equivalents) sodium ascorbate, added 37 seconds after the initial N_2O addition to form Cu_Z^o *in situ* at 297 K. Spectra recorded every 0.5 minutes. *Indicates resting 1-hole Cu_Z*, formed by Cu_Z^o decay during the first 37 seconds before ascorbate addition. B) Normalized time dependence of the reduction of Cu_Z^o at 683 nm (red) and oxidized Cu_A at 482 nm (blue). Kinetic fit using Scheme S1 given by dashed lines (R^2 = 0.9970). C) Absorption spectra of the reduction of resting Cu_Z* (green line) and oxidized Cu_A (blue arrow) by 7.5 mM (~400 equivalents) sodium ascorbate at 297 K, spectra recorded every 1 minute. D) Normalized time dependence of the reduction of oxidized Cu_A at 482 nm (blue) and lack of reduction of resting 1-hole Cu_Z* at 653 nm (green). Kinetic fit using Scheme S3 given by dashed lines (R^2 = 0.9129).

qualitatively consistent with either the rapid reduction of Cu_Z^o via electron transfer from Cu_A or the direct reduction of Cu_Z^o by sodium ascorbate at a very similar rate to the sodium ascorbate reduction of Cu_A. To determine whether Cu_Z^o is reduced via intramolecular electron transfer from Cu_A or by direct reduction by sodium ascorbate, kinetic models for both potential pathways were developed (Schemes S1 and S2 respectively, and Supporting Discussion). Both models contain seven steps: the bimolecular reduction of Cu_A by ascorbate (in the presence of Cu_Z^o, Cu_Z*, or the fully reduced cluster), reduction of Cu_Z^o (either reversibly by Cu_A in Scheme S1 or irreversibly by ascorbate in Scheme S2), and decay of Cu_Z^o to Cu_Z* (independent of the redox state of Cu_A). The bimolecular rate of reduction of Cu_A by sodium ascorbate can be experimentally determined in the presence of Cu_Z* to be 1.4 M^{-1} s^{-1} (Figure 5D and Scheme S3). The rate of Cu_Z^o decay can also be experimentally determined, in the absence of sodium ascorbate, to be 1.8×10^{-3} s^{-1} (Figure S6). As discussed in the Supporting Information, the reductions of Cu_Z^o and Cu_A by sodium ascorbate were fitted with both models, starting from these experimental values. The model that includes IET provides a good fit for the data with minimal (~35%) perturbation of the experimentally determined bimolecular rate of Cu_A reduction by sodium ascorbate (dashed lines in Figure 5B), while to obtain a similar fit with the direct reduction model the bimolecular rate of reduction of Cu_A by sodium ascorbate in the presence of Cu_Z^o must be reduced by an order of magnitude (Figure S8). This large perturbation in the rate of reduction of Cu_A in the presence of Cu_Z^o versus resting 1-hole Cu_Z* is not chemically reasonable, since the two sites differ only in the position of the edge hydroxide ligand (*vida infra*), which is ~7 Å away from Cu_A. Thus, these data support that reduction of Cu_Z^o occurs via intramolecular electron transfer from Cu_A.

Using the IET kinetic model (Scheme S1), we obtain a lower limit of 0.1 s^{-1} for electron transfer rate from Cu_A to Cu_Z^o. The fit requires that the electron transfer step be reversible with a K_{IET} of 2.5, indicating that Cu_Z^o and Cu_A have similar redox potentials. Reversible electron transfer is also observed in other enzymes with multiple copper sites, *e.g.* the multicopper oxidases.[37] This contrasts with the sodium ascorbate reduction of Cu_A in the presence of resting 1-hole Cu_Z*, where the absorption features of oxidized Cu_A (Figure 5C and 5D, blue) immediately decay but those of resting 1-hole Cu_Z* remain (Figure 5C and D, green). A kinetic model allowing for the possibility of electron transfer from Cu_A to Cu_Z* (Scheme S3) yields an upper limit for k_{IET} of 1×10^{-5} s^{-1} for the unobserved reduction of 1-hole Cu_Z* by Cu_A (Figure 5D, dashed lines). This shows that the rate of Cu_A reduction of Cu_Z^o is at least 10^4 faster than the reduction of 1-hole Cu_Z* by Cu_A. The

origin of this difference in electron transfer rates will be considered below. The reduction of Cu_Z^o by Cu_A using a physiologically relevant reductant establishes that Cu_Z^o can be the oxidized form of the enzyme that participates in turnover *in vivo*, while resting 1-hole Cu_Z*, which cannot be reduced by Cu_A, is an inactive state that does not participate in reactivity.

Note that the above analysis of reduction of Cu_A and Cu_Z^o by sodium ascorbate reflect experimental results up to 800 seconds, at which point complete reduction of Cu_A and Cu_Z^o is observed. After 800 seconds, a second phase of reactivity is observed, in which there is slow growth of an absorption feature at 16,000 cm^{-1} (Figure S9A). This is consistent with a slow one electron oxidation of the fully reduced Cu_4S cluster to resting 1-hole Cu_Z*. No comparable growth at 16,000 cm^{-1} (*i.e.*, oxidation to form resting 1-hole Cu_Z*) is observed during turnover of *Mh*N_2OR with sodium ascorbate, performed by premixing fully reduced *Mh*N_2OR and sodium ascorbate before addition of N_2O (Figure S9B). This indicates that the slow one electron oxidation of the Cu_4S cluster observed after reduction of Cu_Z^o and Cu_A by sodium ascorbate (Figure S9A), possibly due to excess N_2O, is a side reaction that is not relevant to turnover.

3.2.2 Steady-state kinetics: The steady-state turnover of *Mh*N_2OR was studied at different temperatures to obtain thermodynamic parameters for the rate-determining step. The initial rate of oxidation of methyl viologen was used to obtain a plot of ln(k) vs 1/T (Figure 6A) that was fit to the Arrhenius equation using a linear regression analysis to obtain a ΔE_A of 10±2 kcal/mol (see Table S2). Similarly, ln(k/T) *vs* 1/T was plotted (Figure 6B) and fit to the Eyring equation to obtain a $\Delta H^{\ddagger}$ of 10±1 kcal/mol and $\Delta S^{\ddagger}$ of -13±1 cal mol^{-1} K^{-1} (see Table S2). This yields a $\Delta G^{\ddagger}$ at room temperature of 13±2 kcal/mol (see Supporting Information), consistent with the $\Delta G^{\ddagger}$ predicted based on the k_{cat} of *Mh*N_2OR (k_{cat} = 320 s^{-1} at 293 K, corresponding to a $\Delta G^{\ddagger}$ of 13 kcal/mol). The small value obtained for $\Delta S^{\ddagger}$ indicates that the rate-limiting step of turnover does not involve either binding of N_2O or loss of N_2. The specific activity of *Mh*N_2OR shows a bell-shaped dependence on pH and pD (Figure 7). The enzyme attains optimum activity at pH ~8 and loses activity at lower and higher pH with pKa values of 6.19±0.05 and 9.15±0.05. The lower value is consistent with the pKa determined in a previous study of the intermolecular rate constant between *Mh*N_2OR and reduced methyl viologen.[26] The pKa values are shifted by 0.2 and 0.3 log units, respectively, when the steady-state turnover experiments are performed in deuterated buffer. A small solvent kinetic isotope effect (SKIE) of 1.12±0.06 is observed at optimum pH, indicating that a solvent exchangeable proton contributes to the transition state in the rate determining step but is not significantly transferred. The temperature dependence of the initial rate of N_2O reduction shows no significant variation outside of error when performed at three different pH values (Figure 6), indicating that the same species is responsible for activity at all pH's. Thus, the bell-shaped pH profile of activity reflects protonation equilibria between three species, where only the species present at intermediate pH is active. The inactive high pH species can

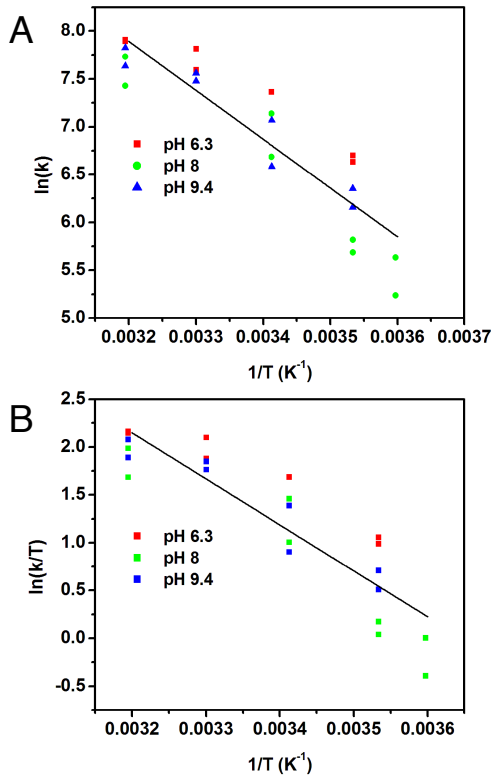

Figure 6: Temperature dependence of the initial rate of methyl viologen consumption during steady-state turnover of N_2OR. A) Arrhenius plot, with linear regression fit (R^2 = 0.8298). B) Eyring plot, with linear regression fit (R^2 = 0.8119). Colors indicate temperature dependence data at different pH values: pH 6.3 (red), pH 8.0 (green) and pH 9.4 (blue).

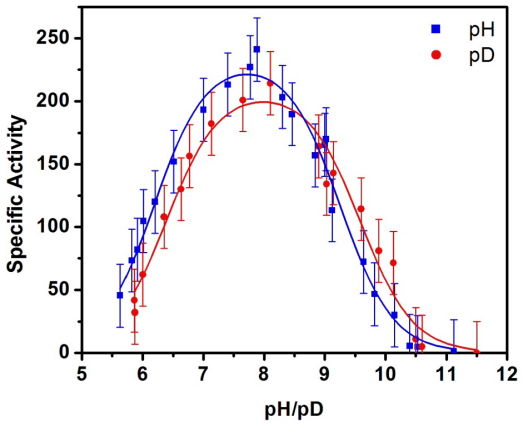

Figure 7: The pH and pD profiles of steady-state activity of *Mh*N_2OR at 297 K in μmol N_2O min^{-1} mg^{-1}, fit with a speciation curve generated by pKa(H) values of 6.19±0.05 and 9.15±0.05 (blue) and pKa(D) values of 6.4±0.1 and 9.5±0.1, with a solvent deuterium isotope effect of 1.12±0.06 (red).

be assigned as having Lys397 deprotonated, since the pKa of 9.15 determined for loss of activity at high pH is identical to that determined for Lys397 based on the pH dependence of the spectral features of resting 1-hole Cu_Z* and its

reduction.[20] The pKa value of 6.19 corresponds to that expected for the second protonation of a His sidechain but no changes in the absorption features of oxidized Cu_A or resting 1-hole Cu_Z* are observed between pH 7.6 and pH 5 (Figure S10), indicating that the protonation does not occur at one of the copper sites in the resting state. It is possible that the residue being protonated affects the conformation of the protein or that the pKa is associated with a His in some reduced state in turnover (*e.g.* reduced Cu_A or the fully reduced Cu_4S cluster).

3.3 Calculations.

3.3.1 Model of Cu_Z^o relative to Cu_Z*: spectral assignments. DFT calculations were performed to assess possible structural models for the Cu_Z^o intermediate and evaluate their correlation to the spectroscopic features observed experimentally. A viable model for Cu_Z^o must reproduce the observed shift of the unpaired spin density from dominantly on Cu_I in resting 1-hole Cu_Z* to more on Cu_{IV}, the shift in the Cu-S vibrations of the cluster to higher energy, and the presence of a solvent O^{18} isotope effect on a Cu-S vibration (indicating the presence of a solvent derived edge ligand). Possible models for Cu_Z^o were obtained by evaluating chemically reasonable perturbations to a spectroscopically calibrated model of resting 1-hole Cu_Z* (with protonated Lys397). Resting 1-hole Cu_Z* was modeled well with a hydroxide ligand asymmetrically bridging the Cu_I-Cu_{IV} edge, closer to Cu_I than Cu_{IV} (2.00 and 2.09 Å, Figure 8A). The model includes two second

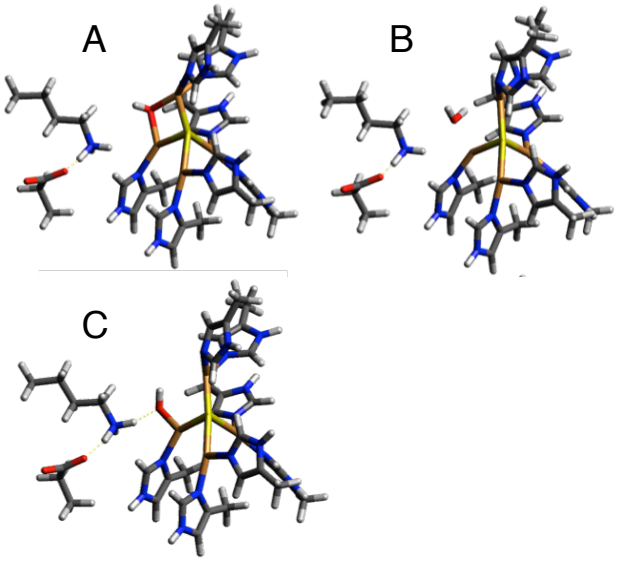

Figure 8: Optimized structures of 1-hole Cu_4S models with different edge ligation. A) Hydroxide bridged model for resting 1-hole Cu_Z*, B) water edge ligand, and C) hydroxide coordinated terminally to Cu_{IV} and hydrogen bonded to Lys397. B) and C) are assessed as possible models for the Cu_Z^o intermediate. (B3LYP, tzvp on Cu_4SON_7, NH_3^+ and CO_2^-, sv on remainder, PCM=10).

sphere residues, Lys397 and Glu435, that are hydrogen-bonded to each other and near to Cu_{IV}, such that Lys397 is 4.02 Å from the μOH. This is extended from our previous computational model, which only included Lys397.[20] When Lys397 in the previous model was protonated, it moves significantly from its crystallographic position to hydrogen bond to the edge hydroxide, which then coordinates directly to Cu_I instead of bridging Cu_I and Cu_{IV}.[20] The present model reproduces the previously observed spectroscopic data for resting 1-hole Cu_Z*, including the minimal perturbation at high pH when Lys397 is deprotonated,[20] without requiring Lys397 to move from its crystallographically defined position (see Supporting Information).

First, possible models of Cu_Z^o resulting from protonation or deprotonation of the edge hydroxide in resting 1-hole Cu_Z* were considered. Protonation results in a model with a water ligand on the Cu_I-Cu_{IV} edge, closer to Cu_{IV} than Cu_I (Figure 8B), while deprotonation to form a bridging oxo leads to proton transfer from Lys397 and results in a μOH and deprotonated Lys. The latter is the same model as was developed in Ref. [20] for the high pH form of resting 1-hole Cu_Z*, which is not active in turnover, and excluded as a model for Cu_Z^o. In the protonated model, the water binds weakly on the Cu_I-Cu_{IV} edge, 2.26 Å from Cu_{IV} and 3.39 Å from Cu_I. Lys397 remains close to its crystallographic position and does not interact with the water edge ligand (Table S4). An additional model was evaluated resulting from a perturbation of the *position* of the hydroxide ligand on the Cu_I-Cu_{IV} edge. By positioning the hydroxide ligand near Cu_{IV} and protonated Lys397, a structure was obtained with a terminal hydroxide ligand coordinated to Cu_{IV} (Cu-O bond length of 1.93 Å) and directly hydrogen bonded to Lys397, which remains in its crystallographic position and hydrogen bonded to Glu435 (Figure 8C). The effects of these perturbations on the calculated spin distribution and vibrations were used to determine which of these models is consistent with the spectral features of Cu_Z^o relative to those of resting 1-hole Cu_Z*.

The calculated Mulliken atomic spin density for the OH_2 model and the Cu_{IV}-OH model, relative to our OH^- bridged model for resting 1-hole Cu_Z*, are given in Table 2. In the OH_2 model, the spin density decreases on Cu_I (from 26% to 8%) and increases on Cu_{II} (12% to 26%), while the spin on Cu_{IV} remains constant. The Cu_{IV}-OH model shows a similar decrease in spin density on Cu_I (26% to 7%) and a threefold

Table 2: Mulliken atomic spin density distribution for computational 1-hole Cu_4S models with different Cu_I-Cu_{IV} edge ligation, given in Figure 8 (B3LYP, tzvp on Cu_4SON_7, NH_3^+ and CO_2^-, sv on remainder, PCM=10).

Edge Ligand	Mulliken Atomic Spin Density					
	Cu_I	Cu_{II}	Cu_{III}	Cu_{IV}	S^{2-}	O
OH^- bridge	0.26	0.12	0.07	0.12	0.26	0.08
OH_2	0.08	0.26	0.13	0.12	0.24	0.00
Cu_{IV}-OH	0.07	0.15	0.03	0.32	0.21	0.10

increase in spin density on Cu_{IV} (12% to 32%), with no significant change on Cu_{II}. Thus, only the Cu_{IV}-OH model reproduced the shift in spin density from Cu_I to Cu_{IV} observed in the absorption and MCD spectra. In this model the unpaired

spin is delocalized ~2:1 over Cu_{IV} and Cu_{II}. This is more localized than is observed for the Cu_Z^o intermediate experimentally based on the EPR hyperfine values, which indicate a 1:1 distribution of spin over two coppers. This suggests that the Cu_{IV}-OH model, while reproducing the spin density shift, overestimates the strength of the ligand field on Cu_{IV}. This effect could arise from the hydrogen bond from Lys397 to the hydroxide being weaker in the model than in the protein, leading to a stronger hydroxide-Cu_{IV} interaction. This would result from an overly strong interaction between the negatively charged Glu435 and the Lys, since there are other hydrogen bonding interactions with Glu435 present in the crystal structure (from a backbone amide and a localized water molecule) that are not included in the computational model.

Experimentally, the Cu_Z^o intermediate is characterized by two vibrations at 426 and 413 cm^{-1} (split by 13 cm^{-1}) where the lower energy vibration shows a -3 cm^{-1} solvent O^{18} isotope shift. The highest energy Cu-S stretch in Cu_Z^o is shifted up in energy by 47 cm^{-1} relative to resting 1-hole Cu_Z*. The energies of the predicted Cu-S and Cu-OH/OH_2 vibrations for the possible models of Cu_Z^o compared to the resting 1-hole Cu_Z* model are given in Table S5. In the resting 1-hole Cu_Z* model, the highest energy core Cu-S vibration occurs at 340 cm^{-1} (378 cm^{-1} experimentally) and has dominant Cu_{II}-μ_4S and Cu_{IV}-μ_4S stretching character. In both possible models for Cu_Z^o, this vibration shifts up in energy due to a significant decrease in the Cu_{IV}-μ_4S bond length (from 2.25 Å to 2.19 Å in both models). For the OH_2 model, a localized Cu_{IV}-S stretch is predicted at 392 cm^{-1}, while in the Cu_{IV}-OH model this vibration occurs at 386 cm^{-1} (52 and 44 cm^{-1} higher in energy than the Cu_{IV}-S vibration of resting 1-hole Cu_Z*, respectively). While both models predict the increased energy of Cu-S vibrations with Cu_{IV}-S stretching character, only the Cu_{IV}-OH model is consistent with the solvent O^{18} isotope shift present in the Cu_Z^o intermediate. In the OH_2 model the Cu_{IV}-S stretch shows no predicted shift with O^{18}, while a -2 cm^{-1} shift is predicted in the Cu_{IV}-OH model. This difference results from greater mixing between the Cu_{IV}-S and Cu_{IV}-OH modes in the Cu_{IV}-OH model because the Cu_{IV}-OH stretch is higher in energy and thus closer in energy to the Cu_{IV}-S stretch (Cu_{IV}-O of 467 cm^{-1} in the Cu_{IV}-OH model and 202 cm^{-1} in the OH_2 model, both with O^{18} shifts of -16 cm^{-1}). This reflects the shorter Cu_{IV}-OH bond relative to the Cu_{IV}-OH_2 bond (1.93 Å versus 2.26 Å).

Thus, the correlations of the predicted spin density distribution and vibrations of OH_2 and Cu_{IV}-OH models with the spectral features of Cu_Z^o support modeling Cu_Z^o as an intermediate with a terminal hydroxide ligand coordinated to Cu_{IV} and hydrogen bonding to a protonated Lys397. This is consistent with the experimental pKa of Lys397 in resting 1-hole Cu_Z* of 9.2, which would only be increased by an additional hydrogen bond to the hydroxide in the Cu_{IV}-OH model, indicating that at the pH of 7.6, used for the spectroscopy of Cu_Z^o, Lys397 will be protonated. While the Cu_{IV}-OH structure is at a local minimum with all real vibrational frequencies (aside from those resulting from the fixed atoms that model the connections to the protein backbone), this Cu_Z^o model is 6.4 kcal/mol higher in free energy than the OH bridged model of resting 1-hole Cu_Z*. Thus, the Cu_Z^o intermediate is a metastable 1-hole form of the cluster formed as the kinetic product of turnover, which decays to the thermodynamically favored resting 1-hole form of Cu_Z*. The rate of decay of Cu_Z^o to resting 1-hole Cu_Z* observed experimentally is 5×10^{-3} s^{-1}, which gives a $\Delta G^{\ddagger}$ of ~20 kcal/mol. We calculate a transition state with a $\Delta G^{\ddagger}$ of 6 kcal/mol (Figure S13) for breaking the hydrogen bond between Lys397 and the Cu_{IV}-OH to form the hydroxide bridge interacting with Cu_I (with a constrained Cu_I-Cu_{IV} distance). We expect this to be a lower limit as the hydrogen bond in this model appears to be weak relative to experiment, due to an overly strong interaction between Lys397 and Glu435 (see above).

3.3.2 Rapid reduction of Cu_Z^o for catalysis: The sodium ascorbate reduction kinetic results presented above demonstrate that Cu_Z^o is rapidly reduced by intramolecular electron transfer from Cu_A, while resting 1-hole Cu_Z* is not, with at least a 10^4-fold greater k_{IET} to Cu_Z^o relative to resting 1-hole Cu_Z*. Using the spectroscopically calibrated models for the Cu_Z^o intermediate and resting Cu_Z* in Figures 8C and 8A, respectively, it is possible to explore the origin of this difference in intramolecular electron transfer rates, which is the basis for the functional role of Cu_Z^o in turnover. Three parameters in Marcus Theory[38] determine the rate of electron transfer: the free energy difference, which provides the driving force for the electron transfer (ΔG^o); the reorganization energy, λ (the sum of inner sphere, λ_i (i.e. bond changes), and outer sphere, λ_o (i.e. solvation changes)); and the electronic coupling between the donor and acceptor sites in the electron transfer process, given by the matrix element H_{DA}. Our computational results indicate that resting 1-hole Cu_Z^o is metastable and +6.4 kcal/mol higher in energy than resting 1-hole Cu_Z*, resulting in an increased driving force for the IET, compared to resting 1-hole Cu_Z*. To evaluate whether a $\Delta\Delta G^o$ of +6.4 kcal/mol is sufficient to account for the >10^4-fold faster electron transfer rate observed experimentally, we determined a value for λ_i using our computational models of Cu_Z^o and resting Cu_Z* (see Supporting Information). The difference between the values obtained for Cu_Z^o and resting 1-hole Cu_Z* is small, so λ_i for these sites can be treated as equal. Based on these computational λ_i values, values for λ_o obtained by comparison to the Cu_A and blue copper sites, and the experimentally determined λ_{total} for Cu_A, a chemically reasonable λ_{total} range of 0.5-1 eV for electron transfer from Cu_A to Cu_Z^o or resting 1-hole Cu_Z* is obtained (see Supporting Information). Since there is no experimental value for H_{DA} for electron transfer from Cu_A to Cu_Z^o or resting 1-hole Cu_Z*, a wide range of possible values (0.001-0.5 cm^{-1}) was considered based on estimates for related sites (see Supporting Information). Using these values, we calculate a range of $\Delta\Delta G^o$ values in the limit where H_{DA} and λ for ET from Cu_A to Cu_Z^o and from Cu_A to resting 1-hole Cu_Z* are equal. This analysis indicates that a $\Delta\Delta G^o$ of 5-10 kcal/mol is sufficient to produce a 10^4-fold faster electron transfer rate from Cu_A to Cu_Z^o, which is consistent with the calculated ΔG of +6.4 kcal/mol of Cu_Z^o relative to resting 1-hole Cu_Z*. Thus, the origin of the >10^4-fold increase in the rate of electron transfer from Cu_A to Cu_Z^o relative to resting 1-hole Cu_Z* is thermodynamic, and the role of the hydrogen-bonded second sphere Lys397 is to

stabilize the metastable Cu_Z^o intermediate to provide the driving force required for rapid reduction of the 1-hole oxidized state during catalysis.

3.3.3 Reaction Coordinate for N-O Bond Cleavage: Having determined from spectroscopy and DFT calculations that the Cu_Z^o intermediate is terminal hydroxide coordinated to Cu_{IV} and stabilized by a hydrogen bond from Lys397, we extended our computational model to evaluate the insight this intermediate gives into the nature of the two electron transfer from the Cu_4S cluster required to break the N-O bond. Previous computational studies of the reaction mechanism of N_2OR have predicted that the product of N-O bond cleavage is a 2-hole intermediate with a μ-oxo or hydroxo ligand bridging the Cu_I-Cu_{IV} edge, with one electron transferred from Cu_{IV} to N_2O at the transition state and the other from Cu_I upon the formation of the Cu_I-O bond of the bridged product.[8,34] However, upon subsequent protonation and reduction, these species would yield inactive resting 1-hole Cu_Z* (i.e., a 1-hole cluster with a μ-hydroxo edge ligand), rather than the reactive 1-hole Cu_{IV}-OH Cu_Z^o intermediate identified above. Using the experimentally validated computational models of 1-hole Cu_Z^o and resting 1-hole Cu_Z* from Section 3.3.1, we have explored the reaction coordinate for N-O bond cleavage, and subsequent protonation and reduction, to determine how the Cu_Z^o intermediate arises from N-O bond cleavage.

N_2O coordination to the fully reduced cluster results in a linear N_2O molecule terminally N-coordinated to Cu_I. However, upon N-O bond elongation by 0.1-0.2 Å to start the N-O bond cleavage reaction, the structure rearranges to form a μ-1,3 coordination geometry (Figure 9A), with the O of N_2O coordinating to Cu_{IV} and hydrogen-bonded to Lys397. This suggests that the N-O bond cleavage reaction proceeds via the μ-1,3 isomer, consistent with the formation of a terminal Cu_{IV}-OH intermediate as the product. Using B3LYP, there is no stable structure for the μ-1,3 isomer (see Supporting Information). To investigate N-O bond cleavage from a stable μ-1,3 isomer, we performed additional calculations on the same structural model with the functional BP86 with 10% Hartree-Fock exchange (hereafter called B10HFP86, see Supporting Information). In the μ-1,3 isomer, backbonding is evident from Cu_I and Cu_{IV} into the N_2O π* orbital that is in the $Cu_I/Cu_{IV}/S/Cu_{II}$ plane (ip), at a lower energy due to the bent N-N-O angle of 135° (Figure 9B, Table S5). This lowers the energy of the N_2O π* orbital that will receive the two electrons involved in N-O bond cleavage.

Upon N-O bond elongation (B10HFP86), a transition state (TS) for N-O bond cleavage is obtained at an N-O bond length of 1.81 Å (Figure 9C, 1.68 Å for B3LYP). This TS occurs at a $\Delta G^{\ddagger}$ of 17.7 kcal/mol and a $\Delta E^{\ddagger}$ of 6.1 kcal/mol (relative to fully reduced and free N_2O; 17.3 kcal/mol and 10.3 kcal/mol, respectively, for B3LYP). These values are in the range of the experimental values of $\Delta G^{\ddagger}$ = 13±2 kcal/mol and $\Delta H^{\ddagger}$ = 10±1 kcal/mol determined for the rate determining step of N_2O reduction. At the TS, the distance between the N of Lys397 and the O of N_2O has decreased from 2.92 Å to 2.63 Å, indicating that the strength of the Lys397-O hydrogen bond has

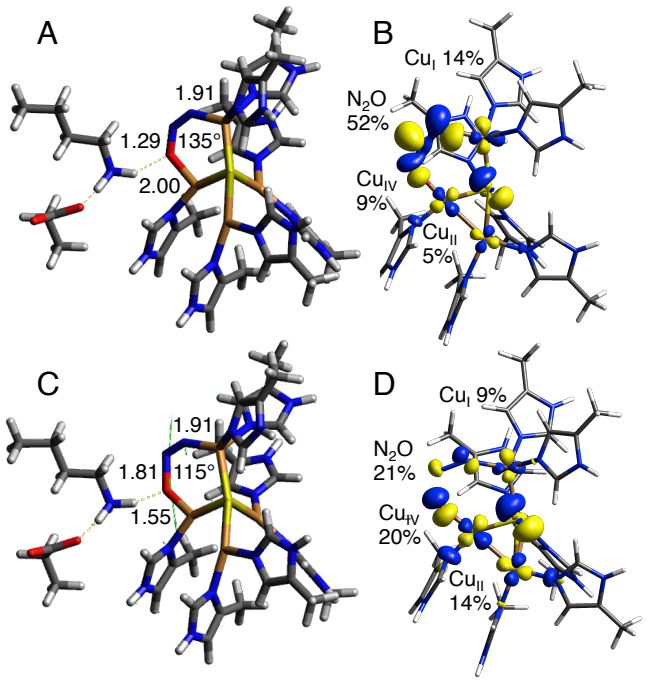

Figure 9: Structures for fully reduced cluster with μ-1,3 N_2O (A) and μ-1,3 TS for N-O bond cleavage (C), giving N-O, O-H, and Cu_I-N bond lengths in Å and the N-N-O angle. Contours for the LUMO of the fully reduced cluster with μ-1,3 N_2O (B) and α LUMO of the μ-1,3 TS (D), with percentage on N_2O, Cu_I, Cu_{II}, and Cu_{IV}. BP86 with 10% Hartree-Fock exchange and PCM of 10.

increased, stabilizing the TS. However, the Lys N-H bond length is still short (1.10 Å at the TS relative to 1.03 Å for the reactants), indicating that the TS is early on the proton transfer coordinate, consistent with the small positive SKIE observed experimentally. We additionally considered the possibility of a transition state formed by μ-1,1-O or terminal Cu_I-O coordination of N_2O, as has been proposed in a previous study.[34] A terminal TS can be found using our model, but it is ~9 kcal/mol higher in energy compared to the μ-1,3 TS, with a $\Delta G^{\ddagger}$ of 26.4 kcal/mol and a $\Delta E^{\ddagger}$ of 19.7 kcal/mol (for B3LYP, see Supporting Information). Additionally, a terminal Cu_I-O or μ-1,1-O-bridged structure would give a bridging oxo or hydroxo product after N-O cleavage, which would result in resting 1-hole Cu_Z* rather than 1-hole Cu_Z^o, where only the latter is capable of turnover. Thus, our model and the experimental identification of the Cu_Z^o intermediate as a terminal Cu_{IV}-OH hydrogen bonded to Lys397 indicate that N-O bond cleavage in nitrous oxide reductase proceeds via the μ-1,3 TS.

The μ-1,3 TS is a broken symmetry singlet, where the α LUMO, which for the reactant is dominantly ipN_2O π* in character (52% N_2O, with 30% Cu from backbonding, Figure 9B and Table S6), is now dominantly Cu and S based (48% Cu character, mostly delocalized over Cu_{IV}, 20%, and Cu_{II}, 16%, via the μ_4S^2, Figure 9D and Table S6). This indicates that an α electron has been transferred from the fully reduced cluster to N_2O at the TS. This is supported by an increase in the Mulliken charge on N_2O from -0.28 in the bound reactant to -0.5 at the transition state (Table S7). The electron has been donated via Cu_{IV}, which has the best

overlap with the N_2O ip π* orbital at the TS, as elongation of the N-O bond in bent N_2O causes polarization of the ip π* orbital towards O relative to the reactants (the dominantly O based N_2O σ* orbital has come down in energy and mixes with the ip π* orbital). Upon further N-O bond elongation past the TS, the α hole becomes delocalized over all four coppers in the cluster and the μ_4S^{2-} (Table S6), lowering the energy of the first electron transfer.

At the TS, the β LUMO remains dominantly N_2O ip π* in character (Table S6), indicating that, as in previous studies, only one electron is required to transfer at the TS to break the N-O bond. The transfer of the second (β) electron to N_2O occurs after the TS, as part of a concerted process involving three bond cleavage and formation steps: N-O cleavage, proton transfer from Lys397 to form an OH ligand at Cu_{IV}, and cleavage of the Cu_I-N bond to release N_2. To determine the factors leading to transfer of the β electron, we performed 3D potential energy surface scans starting from the TS and scanning the N-O, O-H, and Cu_I-N distances in 0.1 Å steps (Figure 10, where the different surfaces correspond to different Cu_I-N distances). These surfaces show that transfer

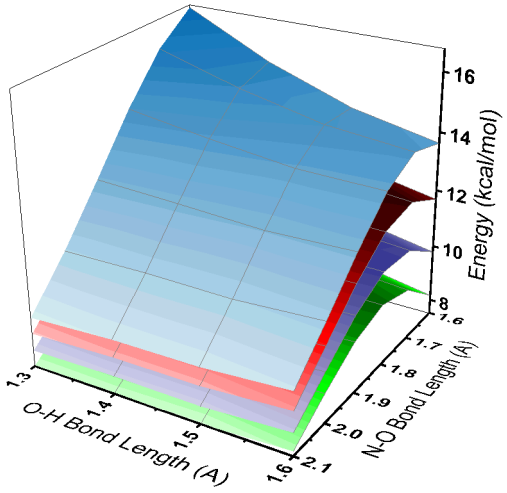

Figure 10: 3D potential energy surfaces for N-O bond cleavage, proton transfer from Lys397 (O-H coordinate), and Cu_I-N bond elongation (BP86 with 10% Hartree-Fock, PCM = 10). Each surface represents a different fixed Cu_I-N distance (2.0 Å green, 2.1 Å purple, 2.2 Å red, 2.3 Å blue). The N-O bond cleavage TS can be seen as a maximum on all surfaces at N-O ~1.7 Å and long O-H bond lengths. Note that O-H transfer only decreases the energy at N-O distances after 2.0 Å.

of the β electron from Cu_{IV} to N_2O occurs together with proton transfer from Lys397 to N_2O, which becomes favorable at an N-O bond distance of 2.1 Å (i.e. 0.3 Å after the TS). The transfer of the β electron is given by the changes in the β LUMO, which reflects uncompensated occupied orbital changes (Figure 11 at right, from top to bottom). At the start of the proton transfer (at N-O 2.1 Å, O-H 1.6 Å, and Cu_I-N 2.0 Å), the β LUMO is mainly oxyl in character (48% O), while the α LUMO is delocalized over Cu_{IV} (20%) and Cu_{II} (19%) (Figure 11A, Table S6, rows 4-5). As the proton transfers from Lys397 and N_2 is released, the β LUMO shifts from the oxyl to Cu_{IV} to

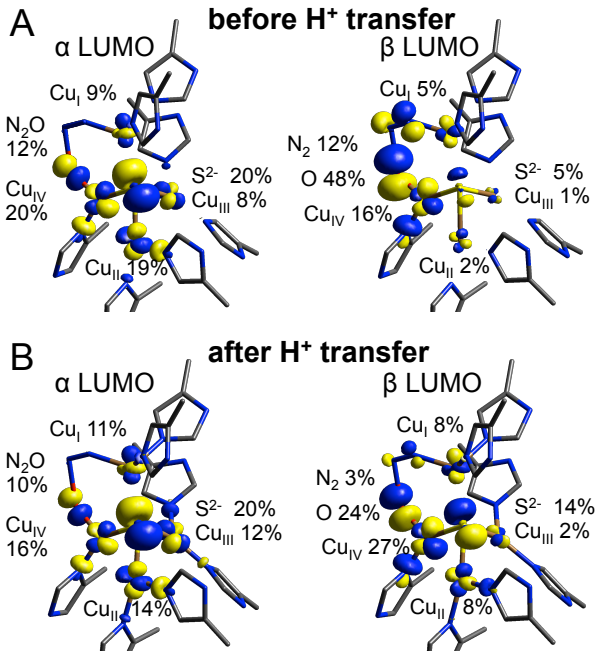

Figure 11: α and β LUMOs before (A) and after (B) proton transfer from Lys397, N-O 2.1 Å, Cu_I-N 2.0 Å.

form a highly covalent Cu_{IV}(II)-OH (24% O and 27% Cu_{IV}, Figure 11B, Table S6, rows 6-7). After this proton transfer, the total Mulliken spin density reflects a broken symmetry singlet with one hole (α) delocalized over Cu_I and Cu_{III} and the second hole (β) over Cu_{IV} and Cu_{II} (Table S8, row 3). Thus, the proton transfer drives the second electron transfer from Cu_{IV} to N_2O during N-O bond cleavage. This emphasizes the importance of the hydrogen bond from Lys397 to N_2O, which provides the proton necessary to trigger the second electron transfer from Cu_{IV}, required to complete the reaction and release N_2.

Subsequent loss of N_2, uptake of a proton from solvent to reprotonate Lys397, and rapid electron transfer from Cu_A are required to stabilize the Cu_Z^o intermediate with a terminally coordinated hydroxide at Cu_{IV} (see Supporting Information). Without this additional proton or electron, loss of N_2 would lead to formation of a μ-hydroxo bridged 2-hole or 1-hole cluster (i.e. Cu_Z*) that would be inactive. This is consistent with the importance of the hydrogen bond from Lys397 in stabilizing the higher energy metastable Cu_{IV}-OH product of N-O cleavage, which is required for rapid reduction of the catalytic site in turnover.

4. Discussion.

In this study, we have shown that the transient 1-hole Cu_Z^o intermediate that initially forms (k_{obs} ~ 200 s^{-1})[23] upon N_2O reduction by fully reduced Cu_4S-containing *Mh*N_2OR can be rapidly reduced by the physiologically relevant electron donor sodium ascorbate. The reduction of Cu_Z^o via electron transfer from Cu_A in turnover with cytochrome c_{552} is faster than the decay of Cu_Z^o to the inactive resting 1-hole Cu_Z* state of the Cu_4S cluster (Scheme 1).[26] This indicates that N_2O reduction by the Cu_4S active site of N_2OR bypasses the resting 1-hole Cu_Z* state, which is not reduced by

physiologically relevant reductants; instead, the 1-hole Cu_Z^o intermediate is the relevant 1-hole oxidized state of the Cu_4S cluster during turnover. Here, we have defined the nature of this 1-hole Cu_Z^o intermediate and elucidated how it differs from the resting 1-hole Cu_Z* state and thus determined the origin of its rapid reduction via Cu_A. Further, the nature of Cu_Z^o produces an important insight into the mechanism of N_2O reduction by the Cu_4S active site of N_2OR and the role of the tetranuclear μ_4S^{2-} bridged cluster in this process.

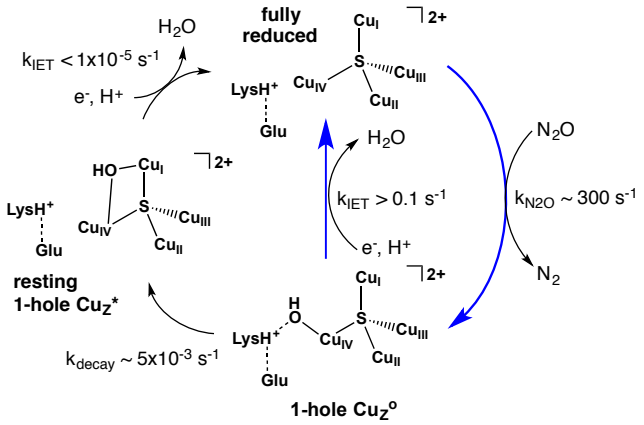

Scheme 1: Pathways of Cu_Z^o formation, reduction, and decay to resting 1-hole Cu_Z* with relevant rates, with blue arrows showing steps involved in catalytic turnover.

4.1 Identification of 1-hole Cu_Z^o and differences with resting 1-hole Cu_Z*. EPR, absorption, MCD and resonance Raman spectroscopies correlated to DFT calculations have been used to develop a model for the 1-hole Cu_Z^o intermediate. The EPR $A_{||}$ values for Cu_Z^o show that the spin is delocalized over two coppers, differing from the ~5:2 distribution of spin over Cu_I and Cu_{IV} observed in resting 1-hole Cu_Z*.[35] Differences in the relative intensities of the μ_4S^{2-} to Cu CT transitions between Cu_Z^o and resting 1-hole Cu_Z* indicate (from the pseudo-A term MCD analysis) that this spin redistribution is due to a decrease in spin density on Cu_I and an increase in spin density on Cu_{IV}. The resonance Raman spectrum of the Cu_Z^o intermediate shows two Cu-S stretching vibrations, an intense mode at 426 cm^{-1} and a weak mode at 413 cm^{-1} which exhibits a -3 cm^{-1} shift when Cu_Z^o is formed in O^{18} labeled water. H_2O^{18} isotope sensitivity in a Cu-S stretching mode indicates that there is a solvent-exchangeable hydroxide ligand on the Cu_I-Cu_{IV} edge, as this leads to Cu-O stretches that are high enough in energy to mix with the Cu-S vibrations of the Cu_4S core. Chemically reasonable models for the Cu_Z^o intermediate were investigated with DFT calculations, and, from correlation to the spectral features of Cu_Z^o, only a Cu_{IV}-OH model stabilized by hydrogen bonding to a protonated second sphere Lys397 reproduces the shift of the spin density from Cu_I to Cu_{IV} and the H_2O^{18} isotope shift in a high energy Cu-S vibration. We thus identify the 1-hole Cu_Z^o intermediate as having a hydroxide ligand bound terminally to Cu_{IV} and hydrogen bonded to Lys397 (Figure 8C and Scheme 1).

This model elucidates the nature of the differences between 1-hole Cu_Z^o (the transient intermediate formed from N_2O reduction) and 1-hole Cu_Z* (the stable resting form that results from Cu_Z^o decay). Both of these 1-hole states of the Cu_4S cluster have a hydroxide edge ligand, but in Cu_Z^o the hydroxide is terminally coordinated to Cu_{IV} (calculated Cu_{IV}-OH of 1.93 Å) while in resting 1-hole Cu_Z* the hydroxide asymmetrically bridges the Cu_I-Cu_{IV} edge, with a stronger interaction with Cu_I than with Cu_{IV} (Cu_I-OH of 2.00 Å, Cu_{IV}-OH of 2.09 Å). The barrier for decay of 1-hole Cu_Z^o to the μOH bridged resting 1-hole Cu_Z* (Scheme 1, bottom) thus arises from breaking the hydrogen bond to Lys397 before the bond with Cu_I is formed. This is consistent with the pH dependence observed for steady-state turnover, which indicates that Lys397 must be protonated for catalytic activity. It also provides an explanation for the reported pH dependence of the turnover-dependent inactivation of *Mh*N_2OR, which suggests that the decay of the Cu_Z^o intermediate is more rapid at higher pH,[27] as deprotonation of Lys397 will lower the barrier for decay of Cu_Z^o to resting 1-hole Cu_Z*.

The key difference in reactivity between the 1-hole Cu_Z^o intermediate and resting 1-hole Cu_Z* is that Cu_Z^o is rapidly reduced in turnover while resting 1-hole Cu_Z* is not. Reduction studies with sodium ascorbate as the electron donor show that 1-hole Cu_Z^o is rapidly reduced via intramolecular electron transfer from Cu_A (with a lower limit on the k_{IET} of 0.1 s^{-1}; to be consistent with the steady-state activity of *Mh*N_2OR, this intramolecular ET rate must be greater than k_{cat} = 320 s^{-1}),[26] while resting 1-hole Cu_Z* is not reduced by electron transfer from Cu_A (with an upper limit on k_{IET} of 1×10^{-5} s^{-1}). The greater than 10^4-fold faster rate of reduction of Cu_Z^o compared to resting 1-hole Cu_Z* reflects the higher energy (calculated at +6.4 kcal/mol) of the metastable Cu_Z^o intermediate, which provides a greater driving force for electron transfer from Cu_A to Cu_Z^o relative to resting 1-hole Cu_Z*. Thus, in turnover the second sphere of the Cu_4S cluster is tuned to stabilize the higher energy Cu_Z^o intermediate, a kinetic product of turnover, so that it has a long enough lifetime that reduction by Cu_A can occur faster than the decay of Cu_Z^o to inactive resting 1-hole Cu_Z*. Importantly, second-sphere stabilization of Cu_Z^o reflects the effect of the Lys397 hydrogen bond to the terminal hydroxide coordinated at Cu_{IV}.

4.2 Mechanistic insight into N_2O reduction. The identification of 1-hole Cu_Z^o as a Cu_{IV}-OH intermediate formed from N-O bond cleavage which can be rapidly reduced by Cu_A produces further insight into the mechanism of N_2O reduction by the Cu_4S cluster in N_2OR. First, it emphasizes the importance of a key asymmetry in the N_2OR active site. The second sphere residue Lys397 is positioned to provide a hydrogen bond only to a ligand coordinated to the Cu_{IV} of the open Cu_I-Cu_{IV} edge. This stabilizes the Cu_Z^o intermediate by creating a barrier to the decay of its terminal Cu_{IV}-OH to form the μOH bridged resting state. The presence of protonated Lys397 near Cu_{IV} also influences the mechanism of N_2O reduction at the Cu_I-Cu_{IV} edge to lead to a non-bridging product. Previous computational descriptions of the reaction coordinate for N-O bond cleavage by the $4Cu^I$ state of

the Cu_4S cluster included either no hydrogen bond donation or hydrogen bond donation by a flexible donor molecule (water or formate).[8,34] These studies proposed several possible modes for N_2O coordination at the Cu_I-Cu_{IV} edge, including terminal O-Cu_I, μ-1,1-O bridging Cu_I and Cu_{IV}, and μ-1,3 bridging (Cu_{IV}-O and Cu_I-N). However, in these reaction coordinate calculations, the product of N-O bond cleavage was either a bridging oxo or hydroxo 2-hole intermediate. Upon subsequent protonation and reduction by Cu_A, these would produce the inactive resting 1-hole Cu_Z* state. In the present study, the reaction coordinate developed in Section 3.3.3 includes the presence of protonated Lys397 and starts with μ-1,3 coordination of N_2O to the fully reduced (Cu^I_4S) cluster. In this binding mode, the Cu_{IV}-O interaction and the Lys397 hydrogen bond is already formed before N-O bond cleavage, precluding the interaction between the O of N_2O and Cu_I. Upon N-O bond cleavage, proton transfer from Lys397, and proton coupled electron transfer from Cu_A, the 1-hole Cu_Z^o intermediate is formed with a terminal hydroxide coordinated to Cu_{IV}. The transition state obtained for this N-O bond cleavage process is consistent with the experimental temperature dependence of the reduction of N_2O by N_2OR under steady-state turnover conditions, which gives the kinetic parameters ΔE_A=10±2 kcal/mol and $\Delta G^{\ddagger}$ =13±2 kcal/mol and a small normal solvent kinetic isotope effect of 1.1 for the rate limiting step. This mechanism is summarized in Scheme 2.

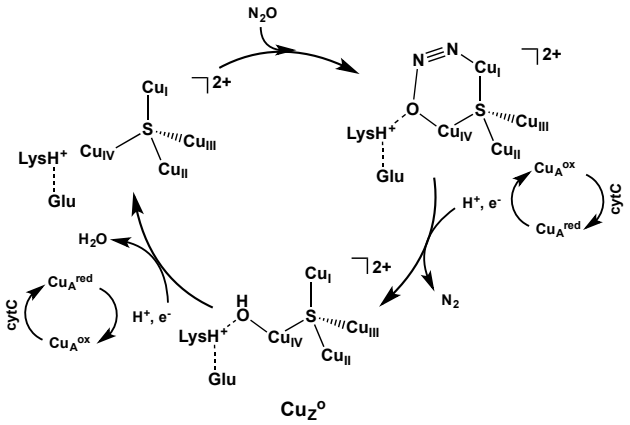

Scheme 2: Mechanism of N_2O reduction by the Cu_4S active site of N_2OR.

4.3 Role of the Cu_4S cluster in N_2O reduction. The formation of a terminal Cu_{IV}-OH intermediate after N-O bond cleavage indicates that the two electron transfer from the $4Cu^I$ cluster required for N_2O reduction proceeds by a significantly different mechanism than previously proposed. Computational studies of N-O bond cleavage with N_2O coordinated between Cu_I and Cu_{IV} indicated that one electron is transferred from Cu_{IV} at the transition state and the other transfers from Cu_I upon formation of the Cu_I-O^{2-} bond later in the reaction coordinate.[8,34] However, the experimentally observed Cu_Z^o intermediate has a terminal hydroxide bound to Cu_{IV} and lacks a Cu_I-O interaction, so in N-O bond cleavage both electrons must be transferred to N_2O via Cu_{IV}.

Examination of the electronic structure changes during N-O bond cleavage (Figure 10 and 11) indicates that this two electron transfer process involves all four coppers in the cluster. The first electron is transferred via Cu_{IV} to break the N-O bond at the transition state. The involvement of Cu_{IV} is due to the increased O character in the N_2O LUMO upon N-O bond elongation. The resulting first electron is delocalized over the other three coppers in the Cu_4S cluster via the μ_4S^{2-} bridge, which provides a good superexchange pathway, lowering the energy of the first electron transfer (Scheme 3A). Subsequently, proton transfer from Lys397 to form the terminal . hydroxide ligand at Cu_{IV} results in the transfer of a second electron, again via Cu_{IV}, which occurs after the N-O bond is broken (Scheme 3B). Proton uptake from solvent and loss of N_2 leads to a 2-hole intermediate where one hole is delocalized over Cu_I and Cu_{III} and the other is delocalized over Cu_{II} and Cu_{IV} (Scheme 3C).

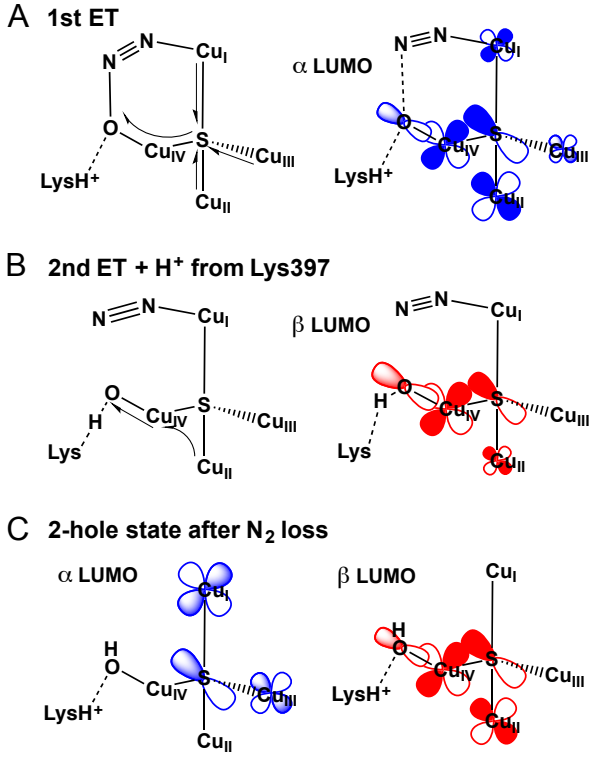

Scheme 3: MO depictions of the first and second electron transfer from the fully reduced ($4Cu^I$) Cu_4S cluster to μ-1,3 N_2O. A) The first electron transfer via Cu_{IV}, B) The second electron transfer via Cu_{IV} with concerted protonation of Lys397, and C) the α and β LUMOs of the product 2-hole Cu_{IV}-OH state.

This mechanism for two electron transfer via a single Cu center elucidates the role of a tetranuclear copper cluster as the active site for N_2OR. In other systems, e.g. the zeolite Cu-ZSM-5, N_2O is reduced by a binuclear copper site with no bridging ligands to provide a superexchange pathway between the copper centers.[44] In the zeolite system, N_2O must coordinate in a μ-1,1-O mode, so that one electron can transfer from one Cu at the TS and the second electron from the other, leading to an oxo bridged product that is active in the zeolite but would be inactive in the N_2OR enzymatic system. To avoid this, the Cu_4S cluster stabilizes the O at Cu_{IV} using second sphere hydrogen bonding and thus has a very

covalent μ_4-bridging sulfide ligand, which provides sufficiently good superexchange that both electrons can be transferred to N_2O via one copper center (Cu_{IV}). While this could potentially be accomplished by a binuclear copper site with a bridging sulfide, our previous computational study of the Cu_4S cluster suggests that the sulfide in a Cu_2S cluster would be highly susceptible to protonation and the resulting μSH would not be an effective superexchange pathway.[8] The presence of two additional coppers in the tetranuclear cluster protects the μ_4S^{2-} from protonation, maintaining the good superexchange that is necessary for two electron transfer via a single copper center.

Thus, the Cu_4S active site of N_2OR is optimized to reduce N_2O asymmetrically, generating a 1-hole intermediate, Cu_Z^o, that has a hydroxide ligand terminally coordinated to Cu_{IV}. Cu_Z^o can be rapidly reduced in turnover via electron transfer from Cu_A, providing a mechanism by which the Cu_4S cluster can reduce N_2O using physiologically relevant electron donors. This excludes the inactive resting 1-hole Cu_Z* state from the catalytic cycle and shows that the Cu_4S form of the N_2OR active site is competent for nitrous oxide reduction *in vivo*.

5. Conclusions. EPR, absorption, MCD and resonance Raman spectroscopies coupled to DFT calculations have defined the nature of the Cu_Z^o intermediate observed in the single turnover reaction of fully reduced N_2OR with N_2O. The Cu_Z^o intermediate has a hydroxide ligand terminally coordinated to Cu_{IV}, stabilized by a second sphere hydrogen bond to the protonated Lys397. The decay of this intermediate, which leads to inactivation of N_2OR, involves breaking the hydrogen bond between Lys397 and the hydroxide to form the μOH bridged resting 1-hole Cu_Z* state. Unlike resting 1-hole Cu_Z*, the 1-hole Cu_Z^o intermediate can be rapidly reduced, via electron transfer from Cu_A, by physiologically relevant reductants. The higher energy of metastable Cu_Z^o relative to resting 1-hole Cu_Z* provides the additional driving force necessary for the rapid reduction of Cu_Z^o in turnover. The terminal hydroxide coordination in Cu_Z^o suggests a mechanism for N_2O reduction by the fully reduced Cu_4S cluster, in which N_2O bridges in a μ-1,3 Cu_{IV}-ON_2-Cu_I structure and the two electrons required for N-O bond cleavage are both transferred through the μ_4S^{2-} bridge via the Cu_{IV} center.

ASSOCIATED CONTENT

Supporting Information. Cu_Z^o spectra with details of Cu_A subtraction; table of bands and assignments for Cu_Z^o and Cu_Z* absorption and MCD spectra; resonance Raman spectrum and profile for resting 1-hole Cu_Z*; kinetic schemes, description of kinetics fitting, and supplemental experiments for Cu_Z^o reduction by ascorbate; description of computational modeling of resting 1-hole Cu_Z*; details of DFT calculations including Cu_4S models for Cu_Z^o and their vibrational assignments; calculated transition state for Cu_Z^o decay; estimates of λ_{total}, H_{DA}, and $\Delta\Delta G^\circ$ for Marcus Theory analysis; additional discussion of the computational reaction coordinate of N-O bond cleavage with 2D PES and tables of Mulliken atomic spin density and Mulliken charges during 2 electron transfer from Cu^I_4S to N_2O; μ-1,1-O TS for N-O cleavage; coordinates for key structures used for DFT calculations. This material is available free of charge via the Internet at http://pubs.acs.org.

AUTHOR INFORMATION

Corresponding Author

* edward.solomon@stanford.edu

Present Addresses

† Department of Chemistry, University of York, York, UK.

‡ Dipartimento di Chimica, Università di Pavia, Via Taramelli 12, 27100 Pavia, Italy.

& Indian Association for the Cultivation of Science, Kolkata, India.

ACKNOWLEDGMENT

This research was supported by the NIH grant DK-31450 (E.I.S.), a Stanford Graduate Fellowship (E.M.J.), and financial support from the Fundação para a Ciência e Tecnologia to IM (PTDC/QUI-BIQ/116481/2010 and PTDC/BBB-BQB/0129/2014) and to CC (SFRH/BD/87898/2012). This work was also supported by the Unidade de Ciências Biomoleculares Aplicadas-UCIBIO, which is financed by national funds from FCT/MEC (UID/Multi/04378/2013) and co-financed by the ERDF under the PT2020 Partnership Agreement (POCI-01-0145-FEDER-007728). SRP is an IF fellow supported by FCT. The content is solely the responsibility of the authors and does not necessarily represent the official views of the National Institutes of Health. The authors declare no competing financial interest.

REFERENCES

(1) Bates, B.; Kundzewicz, Z. W.; Wu, S.; Arnell, N.; Burkett, V.; Döll, P.; Gwary, D.; Hanson, C.; Heij, B.; Jiménez, B.; Kaser, G.; Kitoh, A.; Kovats, S.; Kumar, P.; Magadza, C.; Martino, D.; Mata, L. J.; Medany, M.; Miller, K.; Oki, T.; Osman, B.; Palutikof, J.; Prowse, T.; Pulwarty, R.; Räisänen, J.; Renwick, J.; Tubiello, F.; Wood, R.; Zhao, Z.-C.; Arblaster, J.; Betts, R.; Dai, A.; Milly, C.; Mortsch, L.; Nurse, L.; Payne, R.; Pinskwar, I.; Wilbanks, T.; Secretariat, I., Ed. 2008.

(2) Ravishankara, A. R.; Daniel, J. S.; Portmann, R. W. *Science* 2009, *326*, 123.

(3) Richardson, D.; Felgate, H.; Watmough, N.; Thomson, A.; Baggs, E. *Trends in Biotechnology* 2009, *27*, 388.

(4) Thomson, A. J.; Giannopoulos, G.; Pretty, J.; Baggs, E. M.; Richardson, D. J. *Philosophical Transactions of the Royal Society B-Biological Sciences* 2012, *367*, 1157.

(5) Tavares, P.; Pereira, A. S.; Moura, J. J. G.; Moura, I. *Journal of Inorganic Biochemistry* 2006, *100*, 2087.

(6) Zumft, W. G.; Kroneck, P. M. H. *Advances in Microbial Physiology* 2007, *52*, 107.

(7) Pauleta, S. R.; Dell'Acqua, S.; Moura, I. *Coordination Chemistry Reviews* 2013, *257*, 332.

(8) Gorelsky, S. I.; Ghosh, S.; Solomon, E. I. *Journal of the American Chemical Society* 2006, *128*, 278.

(9) Brown, K.; Djinovic-Carugo, K.; Haltia, T.; Cabrito, I.; Saraste, M.; Moura, J. J. G.; Moura, I.; Tegoni, M.; Cambillau, C. *Journal of Biological Chemistry* 2000, *275*, 41133.

(10) Prudencio, M.; Pereira, A. S.; Tavares, P.; Besson, S.; Cabrito, I.; Brown, K.; Samyn, B.; Devreese, B.; Van Beeumen, J.; Rusnak, F.; Fauque, G.; Moura, J. J. G.; Tegoni, M.; Cambillau, C.; Moura, I. *Biochemistry* 2000, *39*, 3899.

(11) Brown, K.; Tegoni, M.; Prudencio, M.; Pereira, A. S.; Besson, S.; Moura, J. J.; Moura, I.; Cambillau, C. *Nature Structural Biology* 2000, *7*, 191.

(12) Rasmussen, T.; Berks, B. C.; Sanders-Loehr, J.; Dooley, D. M.; Zumft, W. G.; Thomson, A. J. *Biochemistry* 2000, *39*, 12753.

(13) Alvarez, M. L.; Ai, J. Y.; Zumft, W.; Sanders-Loehr, J.; Dooley, D. M. *Journal of the American Chemical Society* 2001, *123*, 576.
(14) Farrar, J. A.; Neese, F.; Lappalainen, P.; Kroneck, P. M. H.; Saraste, M.; Zumft, W. G.; Thomson, A. J. *Journal of the American Chemical Society* 1996, *118*, 11501.
(15) Kroneck, P. M. H.; Kastrau, D. H. W.; Antholine, W. E. *Journal of Inorganic Biochemistry* 1992, *47*, 19.
(16) Psomas, G.; Kessissoglou, D. P. *Dalton Transactions* 2013, *42*, 6252.
(17) Chen, P.; Cabrito, I.; Moura, J. J. G.; Moura, I.; Solomon, E. I. *Journal of the American Chemical Society* 2002, *124*, 10497.
(18) Rasmussen, T.; Berks, B. C.; Butt, J. N.; Thomson, A. J. *Biochemical Journal* 2002, *364*, 807.
(19) Oganesyan, V. S.; Rasmussen, T.; Fairhurst, S.; Thomson, A. J. *Dalton Transactions* 2004, 996.
(20) Ghosh, S.; Gorelsky, S. I.; George, S. D.; Chan, J. M.; Cabrito, I.; Dooley, D. M.; Moura, J. J. G.; Moura, I.; Solomon, E. I. *Journal of the American Chemical Society* 2007, *129*, 3955.
(21) Pomowski, A.; Zumft, W. G.; Kroneck, P. M. H.; Einsle, O. *Nature* 2011, *477*, 234.
(22) Dell'Acqua, S.; Pauleta, S. R.; Moura, J. J. G.; Moura, I. *Philosophical Transactions of the Royal Society B-Biological Sciences* 2012, *367*, 1204.
(23) Johnston, E. M.; Dell'Acqua, S.; Ramos, S.; Pauleta, S. R.; Moura, I.; Solomon, E. I. *Journal of the American Chemical Society* 2014, *136*, 614.
(24) Chan, J. M.; Bollinger, J. A.; Grewell, C. L.; Dooley, D. M. *Journal of the American Chemical Society* 2004, *126*, 3030.
(25) Ghosh, S.; Gorelsky, S. I.; Chen, P.; Cabrito, I.; Moura, J. J. G.; Moura, I.; Solomon, E. I. *Journal of the American Chemical Society* 2003, *125*, 15708.
(26) Dell'Acqua, S.; Pauleta, S. R.; Monzani, E.; Pereira, A. S.; Casella, L.; Moura, J. J. G.; Moura, I. *Biochemistry* 2008, *47*, 10852.
(27) Dell'Acqua, S.; Pauleta, S. R.; Paes de Sousa, P. M.; Monzani, E.; Casella, L.; Moura, J. J. G.; Moura, I. *Journal of Biological Inorganic Chemistry* 2010, *15*, 967.
(28) Frisch, M. J.; Trucks, G. W.; Schlegel, H. B.; Scuseria, G. E.; Robb, M. A.; Cheeseman, J. R.; Scalmani, G.; Barone, V.; Mennucci, B.; Petersson, G. A.; Nakatsuji, H.; Caricato, M.; Li, X.; Hratchian, H. P.; Izmaylov, A. F.; Bloino, J.; Zheng, G.; Sonnenberg, J. L.; Hada, M.; Ehara, M.; Toyota, K.; Fukuda, R.; Hasegawa, J.; Ishida, M.; Nakajima, T.; Honda, Y.; Kitao, O.; Nakai, H.; Vreven, T.; Montgomery Jr., J. A.; Peralta, J. E.; Ogliaro, F.; Bearpark, M. J.; Heyd, J.; Brothers, E. N.; Kudin, K. N.; Staroverov, V. N.; Kobayashi, R.; Normand, J.; Raghavachari, K.; Rendell, A. P.; Burant, J. C.; Iyengar, S. S.; Tomasi, J.; Cossi, M.; Rega, N.; Millam, N. J.; Klene, M.; Knox, J. E.; Cross, J. B.; Bakken, V.; Adamo, C.; Jaramillo, J.; Gomperts, R.; Stratmann, R. E.; Yazyev, O.; Austin, A. J.; Cammi, R.; Pomelli, C.; Ochterski, J. W.; Martin, R. L.; Morokuma, K.; Zakrzewski, V. G.; Voth, G. A.; Salvador, P.; Dannenberg, J. J.; Dapprich, S.; Daniels, A. D.; Farkas, Ö.; Foresman, J. B.; Ortiz, J. V.; Cioslowski, J.; Fox, D. J.; Gaussian, Inc.: Wallingford, CT, USA, 2009.
(29) Hanwell, M. D.; Curtis, D. E.; Lonie, D. C.; Vandermeersch, T.; Zurek, E.; Hutchison, G. R. *Journal of Cheminformatics* 2012, *4*, 17.
(30) Li, Y.; Cirino, P. C. *Biotechnology and Bioengineering* 2014, *111*, 1273.
(31) Humphrey, W.; Dalke, A.; Schulten, K. *"VMD - Visual Molecular Dynamics"*, 1996; Vol. 14.
(32) Tenderholt, A. L. *QMForge: A Program to Analyze Quantum Chemistry Calculations*; Version 2.3.2 ed.
(33) Park, K.; Solomon, E. I. *Canadian Journal of Chemistry* 2014, *92*, 975.
(34) Ertem, M. Z.; Cramer, C. J.; Himo, F.; Siegbahn, P. E. M. *Journal of Biological Inorganic Chemistry* 2012, *17*, 687.
(35) Chen, P.; George, S. D.; Cabrito, I.; Antholine, W. E.; Moura, J. J. G.; Moura, I.; Hedman, B.; Hodgson, K. O.; Solomon, E. I. *Journal of the American Chemical Society* 2002, *124*, 744.
(36) Johnston, E. M.; Dell'Acqua, S.; Pauleta, S. R.; Moura, I.; Solomon, E. I. *Chemical Science* 2015, *6*, 5670.
(37) Heppner, D. E.; Kjaergaard, C. H.; Solomon, E. I. *Journal of the American Chemical Society* 2014, *136*, 17788.
(38) Marcus, R. A.; Sutin, N. *Biochimica Et Biophysica Acta* 1985, *811*, 265.
(39) Auer, B.; Fernandez, L. E.; Hammes-Schiffer, S. *Journal of the American Chemical Society* 2011, *133*, 8282.
(40) Fernandez, L. E.; Horvath, S.; Hammes-Schiffer, S. *Journal of Physical Chemistry C* 2012, *116*, 3171.
(41) Heppner, D. E.; Kjaergaard, C. H.; Solomon, E. I. (unpublished work).
(42) Gamelin, D. R.; Randall, D. W.; Hay, M. T.; Houser, R. P.; Mulder, T. C.; Canters, G. W.; de Vries, S.; Tolman, W. B.; Lu, Y.; Solomon, E. I. *Journal of the American Chemical Society* 1998, *120*, 5246.
(43) Bar-Nahum, I.; Gupta, A. K.; Huber, S. M.; Ertem, M. Z.; Cramer, C. J.; Tolman, W. B. *Journal of the American Chemical Society* 2009, *131*, 2812.
(44) Bhattacharyya, S.; Sarkar, A.; Dey, S. K.; Jose, G. P.; Mukherjee, A.; Sengupta, T. K. *Dalton Transactions* 2013, *42*, 11709.

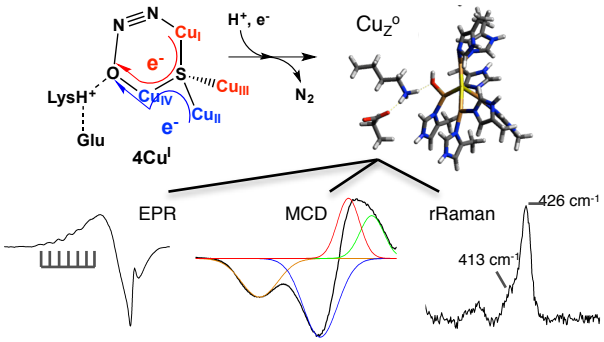
N
N
Cu_I
e-
O
S
Cu_III
LysH+
Cu_IV
Cu_II
e-
Glu
4Cu^I
H+, e-
N2
Cu_Z^o

EPR
MCD
rRaman
426 cm-1
413 cm-1